Pulse Profiles of Accreting Neutron Stars at Low Accretion Rates

Bachelorarbeit aus der Physik

vorgelegt von

Lucia Härer

am 17. September 2019

Astronomisches Institut Dr. Karl Remeis-Sternwarte
Friedrich-Alexander-Universität Erlangen-Nürnberg

Betreuer: Prof. Dr. Jörn Wilms

Abstract

Neutron stars accreting matter from a companion star in a binary system can exhibit periodic variations in their flux. These so-called X-ray pulsars provide an opportunity to study highly magnetized plasma and general relativity observationally. This thesis models pulse profiles of highly magnetized ($B = 10^{11}$–$10^{13}\,\mathrm{G}$) X-ray pulsars at low accretion rates of $\dot{M} \lesssim 10^{15}\,\mathrm{g\,s^{-1}}$, for which the accreting plasma is mainly stopped by Coulomb collisions in the neutron star's atmosphere, resulting in a hot spot-like emission region. The modeling is based on the `polcap` model and the `LIBANS` code. The `polcap` model gives the angular and spectral distribution of the emitted X-rays, by solving polarized radiative transfer of X-ray photons in the neutron star's atmosphere. The `LIBANS` code accounts for changes in the photon trajectories due to relativistic light bending. The dependence of the pulse profiles on the inclinations of the observer and the magnetic axis, the polarization mode, and the energy is investigated. The modeled pulse profiles show a large variety of shapes, with up to three maxima and minima in one rotational period. A change of 10°–20° in the inclination can impact the pulse profile significantly. The ordinary polarization mode shapes the pulse profile, while the contribution from the extraordinary mode is single-peaked and sinusoidal. The energy dependence is most prominent around the cyclotron energy. These results can provide a foundation for understanding the physical processes on X-ray pulsars, if backed up by future observations.

Deutsche Zusammenfassung

Neutronensterne in einem Doppelsternsystem können Materie von ihrem Begleitstern akkretieren, was periodische Änderungen in ihrem Strahlungsfluss hervorrufen kann. Beobachtungen dieser sogenannten Röntgenpulsare helfen, die Physik stark magnetisierter Plasmen und die Relativitätstheorie besser zu verstehen. In dieser Bachelorarbeit werden Pulsprofile von stark magnetisierten ($B = 10^{11}$–$10^{13}\,\mathrm{G}$) Röntgenpulsaren mit kleinen Akkretionsraten $\dot{M} \lesssim 10^{15}\,\mathrm{g\,s^{-1}}$ modelliert. Bei diesen Akkretionsraten wird das akkretierende Plasma hauptsächlich durch Coulomb-Kollisionen mit Teilchen der Atmosphäre des Neutronensterns gestoppt. Dies führt zur Entstehung einer Hotspot-artigen Emissionsregion. Die Modellierung basiert auf dem `polcap` Modell and dem `LIBANS` Code. Das `polcap` Modell berechnet das Spektrum und die Winkelverteilung der Röntgenstrahlen, indem es den polarisierten Strahlungstransfer für Röntgenphotonen in der Atmosphäre des Neutronensterns löst. Der `LIBANS` Code berücksichtigt den Einfluss relativistischer Effekte auf die Photonentrajektorien. Es wurde die Abhängigkeit der Pulsprofile von der Inklination des Beobachters und der Magnetachse, der Polarisation und der Energie untersucht. Die modellierten Pulsprofile unterscheiden sich teilweise stark und haben bis zu drei Minima und Maxima je Rotationsperiode. Eine Änderung der Inklination um 10°–20° kann die Pulsprofile signifikant beeinflussen. Die ordentliche Polarisationsmode bestimmt die Form des Pulsprofils, während der Beitrag der außerordentliche Mode sinusförmig ist. Die Energieabhängigkeit ist bei der Zyklotronenergie am stärksten. Diese Ergebnisse zeigen, dass Beobachtungen mit Instrumenten, die Polarisation im Röntgenbereich messen können, es erlauben könnten, Modelle für die physikalischen Prozesse in Röntgendoppelsternsystemen zu testen.

Contents

1 Introduction

The history of physics is a history of pushing limits. Often, laws that were thought to be universal get challenged when tested in extreme conditions. In multiple ways, neutron stars are among the most extreme objects in the universe. Not only are they on the verge of collapsing to a black hole, but they also posses magnetic fields of the order of 10^8–10^{14} G and sometimes sub-second spin periods (e.g., Lai 2001; Bissinger 2016, and references therein). For comparison, the highest magnetic fields generated on earth[1] have a strength of $\sim 10^4$ G. A neutron star is the collapsed core of a massive star ($M > 8\,M_\odot$), which exploded in a supernova (e.g., Bissinger 2016, and references therein). Neutron stars have typical masses of $1.4\,M_\odot$ and radii of 10 km (e.g., Lattimer 2012). Theses features make them fascinating objects, which provide a key to testing relativity, plasma physics, and theories about matter in strong magnetic fields.

1.1 X-ray Binaries

We can study neutron stars by means of their light that reaches us. One of the most efficient mechanisms to produce light is the accretion of matter onto a massive and compact object, such as a neutron star. Neutron stars in binary systems can accrete matter from their companion star. Depending on the companion's mass, M, different accretion mechanisms occur. For $M < 2\,M_\odot$, the so-called Low Mass X-ray Binaries (LMXB), Roche-lobe overflow dominates (e.g., Bissinger 2016; Caballero & Wilms 2012, and references therein). In other words, the companion star fills the Roche-lobe of the binary system, causing matter to flow through the Lagrange point L_1 onto the neutron star, forming an accretion disc. Common rotational periods of LMXBs are in the sub-second rage. In contrast, High Mass X-ray Binaries (HMXB) have $M > 8\,M_\odot$ and are powered by the accretion of stellar wind from the companion star (e.g., Bissinger 2016; Caballero & Wilms 2012, and references therein). As these systems contain high mass O or B stars, which spend less time on the main sequence than lighter stars, they are typically younger than LMXBs. This also comes with higher magnetic fields (10^{11}–10^{13} G) of the neutron star, as the field decays over time (Bhattacharya & van den Heuvel 1991; Zhang & Kojima 2006). HMXBs typically have rotation periods ranging from 1 to 1000 seconds. Note that the compact object in a LMXB or HMXB can also be a black hole instead of a neutron star. As this thesis is concerned with accreting neutron stars, this will not be discussed further.

[1] see `https://nationalmaglab.org/about/facts-figures/world-records` on September 3rd, 2019

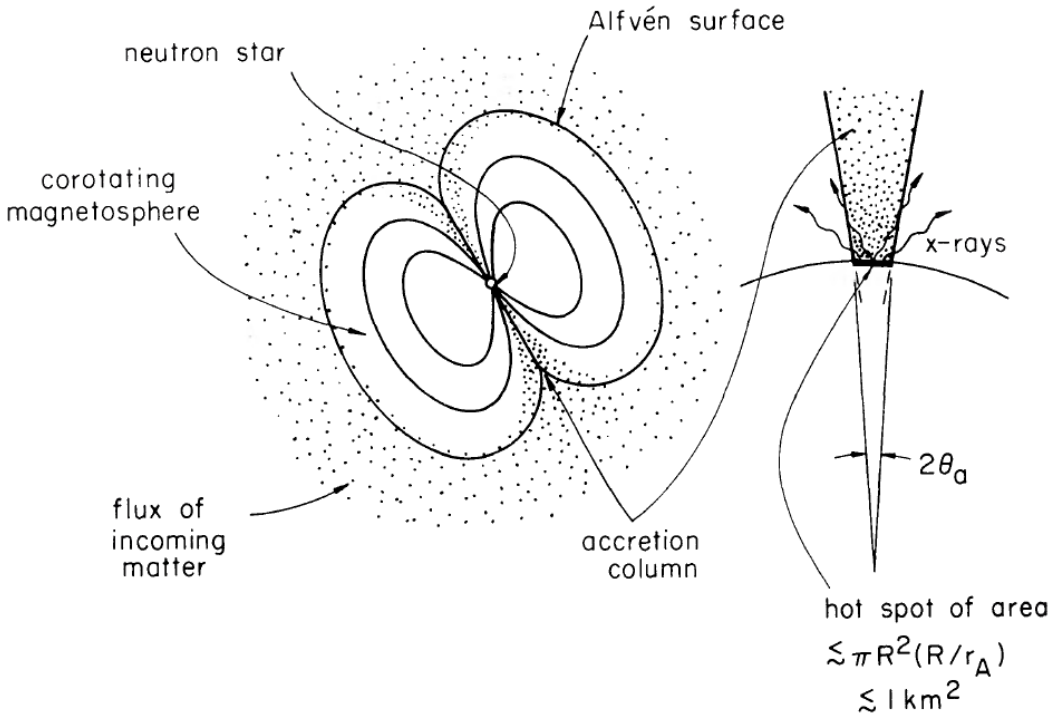

Figure 1.1: Schematic view of an accreting neutron star (Lamb et al. 1973, Fig. 1). On the left hand side, a neutron star with its magnetosphere is shown. The dots indicate incoming matter, which accretes on the magnetic poles, following the field lines inside the Alfvén radius. On the right hand side, accretion on the pole is shown from close up. An estimate for the size of the emission region is given, where r_A is the Alfvén radius and R the radius of the neutron star.

As material falls onto the neutron star, it reaches a radius where its kinetic energy density is equivalent to the energy density of the neutron star's magnetic field. This radius is defined as the Alfvén radius (e.g., Lamb et al. 1973)

$$R_\mathrm{A} = 2.73 \cdot 10^7\,\mathrm{cm} \left(\frac{\Lambda}{0.1}\right) \left(\frac{M_*}{1.4\,M_\odot}\right)^{1/7} \left(\frac{R_*}{10\,\mathrm{km}}\right)^{10/7} \left(\frac{B_*}{10^{12}\,\mathrm{G}}\right)^{4/7} \left(\frac{L_\mathrm{X}}{10^{37}\,\mathrm{erg\,s^{-1}}}\right)^{-2/7}, \tag{1.1}$$

where M_*, R_*, and B_* refer to the mass, radius, and magnetic field strength of the neutron star respectively, L_X is the object's luminosity in X-rays, and Λ is a constant depending on the accretion geometry, e.g., $\Lambda = 1$ for spherical accretion and $\Lambda < 1$ for disc accretion. At a radius $R < R_\mathrm{A}$, inside the so-called magnetosphere, the material is channeled along the field lines to the magnetic poles, where it interacts with the atmosphere and loses its energy to radiation (Lamb et al. 1973), as depicted in Fig. 1.1. The emission is mainly in the X-ray range, due to the high velocity of the accreting matter (see Sect. 2.2 for further discussion).

1.2 Pulse profiles of X-ray pulsars

As described above, neutron stars in binary systems can emit X-rays by accreting matter from their companion star. Some X-ray binaries, the so-called X-ray pulsars, have a flux that varies periodically with time (Giacconi et al. 1971; Tananbaum et al. 1972). This periodic variation occurs if the neutron star's rotational and magnetic axes are not aligned, as the visibility of the magnetic poles changes for the observer in the course of rotation. With Centaurus X-3 (Giacconi et al. 1971) and Hercules X-1 (Tananbaum et al. 1972), the first two X-Ray pulsars were observed in the early 1970s, a decade after the discovery of X-ray binary systems (Giacconi et al. 1962). Today, X-ray pulsars are among the brightest X-ray sources known (e.g., Becker et al. 2012).

The dependence of the flux on the neutron star's angle of rotation is called the pulse profile. In the simplest case the pulse profile is single peaked, i.e., one pulse per rotation is observed. In some cases, pulse profiles can have more complex shapes, like multiple peaks with dissimilar intensities (e.g., Falkner 2018). Various factors impact the pulse profile's shape:

1. The observer's viewing angle, as the emission is localized at the magnetic poles, i.e., not emitted isotropically from the surface.

2. The emission geometry, i.e., the angular and spacial dependence of the emitted photons. The emission geometry depends on physical parameters, such as the accretion rate, $\dot{M}$, and the magnetic field strength, B (see Sect. 2.2).

3. The neutron star's mass, M_{NS}, and radius, R_{NS}, influence how the light trajectories are bent due to general relativity (see Sect. 2.3).

4. Neutron stars are typically assumed to have a dipole field. However, other field geometries cannot be ruled out (Pétri 2019). The field geometry determines the number and location of magnetic poles and therefore the observed pulse profile.

Pulse profiles contain a vast amount of information, due to the variety of factors given above. The study of pulse profiles therefore provides a key to understanding the physical processes on accreting neutron stars. However, the high number of contributing factors makes it difficult to link models with observations. Modeling is a challenge for itself, as the behavior of plasma in high magnetic and gravitational fields has to be understood.

The aim of this thesis is to model pulse profiles of highly magnetized X-ray pulsars ($B = 10^{11}$–$10^{13}\,\mathrm{G}$) at low accretion rates ($\dot{M} \lesssim 10^{-15}\,\mathrm{g\,s^{-1}}$). In doing so, the `polcap` model (Sokolova-Lapa et al. 2019, in prep.), which describes the emission geometry at these accretion rates and field strengths, will be combined with the `LIBANS` code (Falkner 2012, 2018), which accounts for relativistic effects. Chapter 2 covers the theoretical foundation of these models. The models themselves are discussed in Chapter 3, before the results of the analysis are given in Chapter 4 and put into context in Chapter 5.

2 Theory

When matter is accreted onto a neutron star, it interacts with the atmosphere which produces radiation in a localized region on the neutron star's surface, the emission region. The radiation interacts with the surrounding plasma by scattering or absorption processes. These interactions and their effect on the resulting spectrum are described by a radiative transfer equation (Mihalas 1978). The radiation escaping from the emission region eventually reaches the remote observer, after experiencing relativistic effects due to the high mass and compactness of the neutron star.

The aim of this chapter is to describe the theoretical foundation underlying each of the steps above, before introducing the models (see Chapter 3) that were used for the analysis of pulse profiles (see Chapter 4). The behavior of matter in strong magnetic fields is discussed in Sect. 2.1, followed by an overview of emission and propagation of X-rays in the neutron star's atmosphere (Sect. 2.2). To conclude this chapter, relativistic light bending is introduced in Sect. 2.3.

2.1 Matter in strong magnetic fields

Strong magnetic fields affect the structure of matter, as well as radiative transfer. In fields close to the critical field strength of $B_{\mathrm{crit}} = 4.14 \cdot 10^{13}\,\mathrm{G}$, relativistic as well as quantum effects have to be considered. This section gives a brief overview of polarization effects (Sect. 2.1.1) and resonant scattering on Landau levels (Sect. 2.1.2) with regard to accretion on highly magnetized neutron stars, which will be discussed in Sect. 2.2. For a detailed discussion see, e.g., Lai (2001).

2.1.1 Polarization

A photon traveling in a magnetic field, $\mathbf{B}$, can be polarized in two ways with respect to a plane spanned by $\mathbf{B}$ and the photon's wave vector, $\mathbf{k}$. In other words, the polarization vector can either be in the plane or perpendicular to it, as illustrated in Fig. 2.1. The former state is referred to as ordinary mode, the latter as extraordinary mode (e.g., Wang et al. 1988).

The presence of a magnetic field causes a difference in the scattering and absorption cross sections of these modes. This difference is significant for the high fields present on accreting neutron stars and therefore has to be included in radiative transfer models (Wang et al. 1988). Among the effects at play are plasma birefringence and vacuum polarization. Birefringence is known from crystals like calcite, which have different

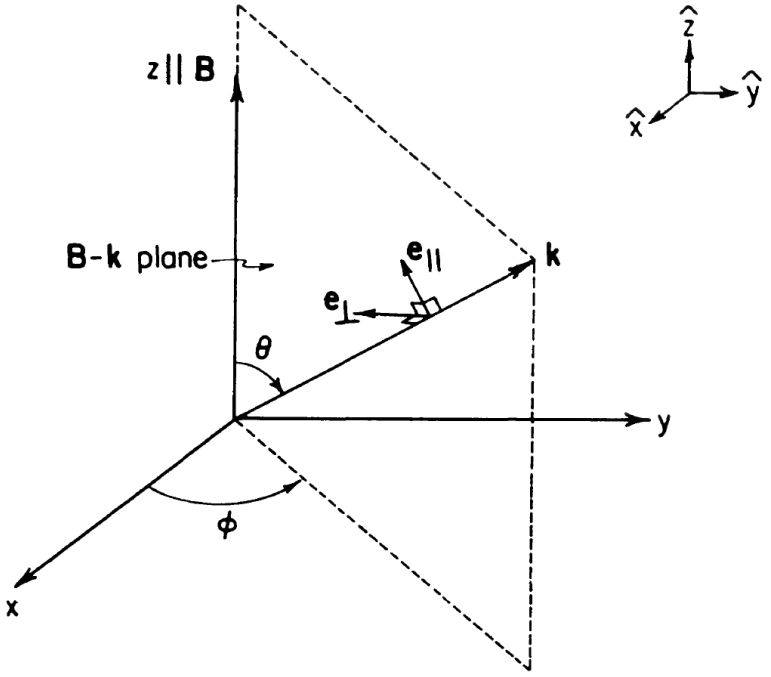

Figure 2.1: The ordinary and extraordinary polarization modes are illustrated (Wang et al. 1988, Fig. 1). **B** indicates the magnetic field and **k** the photon wave vector. The ordinary mode, $\mathbf{e}_{\parallel}$, lies in the **B**-**k** plane, while the extraordinary mode, $\mathbf{e}_{\perp}$, is perpendicular to it.

refractive indices along different axes. An equivalent effect is seen in a plasma, which gets polarized by a magnetic field (e.g., Pavlov et al. 1980). Vacuum polarization refers to the effect that the creation of electron-positron pairs by strong electromagnetic fields has on the fields themselves (Mészáros & Ventura 1978).

2.1.2 Resonant scattering on Landau levels

Resonant scattering on Landau levels is described in detail by, e.g., Lai (2001). This section summarizes the main points.

In magnetic fields, electrons follow circular orbits around the field lines, with a radius given by the Larmor radius

$$\rho = \frac{m_e c v_\perp}{eB}\,, \tag{2.1}$$

where $v_\perp$ is the velocity perpendicular to the magnetic field, B the magnetic field strength, m_e the electron mass, e the elementary charge, and c the speed of light. The frequency of gyration is given by the cyclotron frequency

$$\omega_\mathrm{cyc} = \frac{eB}{m_\mathrm{e} c}\,. \tag{2.2}$$

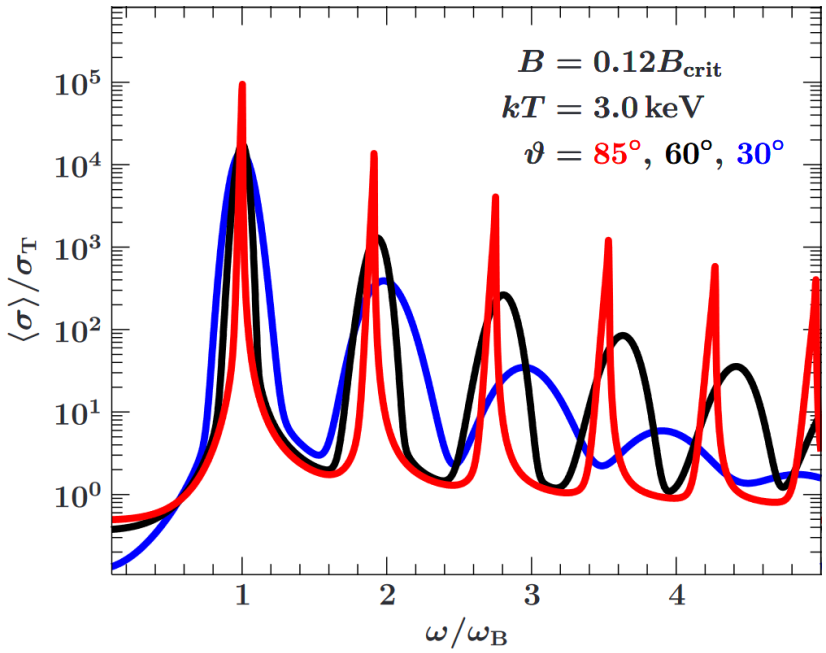

Figure 2.2: Simulated cross section for magnetic Compton scattering (Schwarm et al. 2017b, Fig. B.2). The cross section is given in terms of the Thompson cross section, $\sigma_{\rm T}$. The colors indicate the angle ϑ of the scattering photon with respect to the magnetic field.

At field strengths for which the Larmor radius is of the order of the de Broglie wavelength of electrons, quantum mechanical effects have to be considered. As a result, the electron's movement perpendicular to the magnetic field gets quantized into equidistant Landau levels. In non-relativistic quantum mechanics, the energy of the n-th level is given by (e.g., Lai 2001)

$$E_n^{\rm cyc} = n \cdot \hbar\omega_{\rm cyc} \approx n \cdot 11.58\,{\rm keV}\frac{B}{10^{12}\,{\rm G}}\,, \tag{2.3}$$

which is known as the 12-B-12 rule. In quantum electro dynamics, the Landau levels are not equidistant and slightly shifted. The electron can move freely in parallel to the magnetic field.

The Landau levels allow electrons to undergo resonant scattering with photons. In a plasma, this effect modifies the cross sections of scattering and absorption processes. An important example is inverse Compton scattering, i.e., the upscattering of a photon by a relativistic electron. Note that the term "Compton scattering" refers to the reverse process, where the photon looses energy. The modification of both Compton and inverse Compton scattering by the presence of Landau levels is collectively referred to as magnetic Compton scattering (Schwarm et al. 2017a,b). Its cross section is shown in Fig. 2.2. In

addition to scattering, transitions of electrons between Landau levels are possible by absorption and emission of photons.

The resonant character of magnetic Compton scattering results in dips in the spectra of some X-ray pulsars at E_{cyc} and higher harmonics, the so-called Cyclotron Resonant Scattering Features (CRSFs). As E_{cyc} depends directly on the magnetic field strength, B, the CRSF energy provides a direct measure for B in the region where the radiation is emitted. Note that the observed CRSF can be a sum of contributions from multiple emission regions. CRSFs were first discovered by Truemper et al. (1978) in the X-ray pulsar Her X-1. Since then, multiple observations have been made. In the case of 4U 0115+63, five harmonics have been observed in one source (e.g., Ferrigno et al. 2009, and references therein). Refer to Staubert et al. (2019) for a recent review.

2.2 Accretion physics

As the accreting matter interacts with the atmosphere of the neutron star, different structures form depending on the accretion rate. These structures are described in Sect. 2.2.1, along with mechanisms that are responsible for slowing down the plasma flow and for the emission of X-rays. Radiative transfer and its effect on the spectrum of X-ray pulsars are discussed in Sect. 2.2.2.

2.2.1 X-ray emission

To understand why X-rays are emitted, the stopping of the plasma flow near the neutron star's surface has to be investigated. A crucial parameter is the mass accretion rate, $\dot{M}$, as it determines the amount of radiation that is emitted and therefore, what structures form in the falling plasma (Becker et al. 2012). $\dot{M}$ is related to the luminosity, L, by

$$L(\dot{M}) \sim \frac{G M_{\mathrm{NS}} \dot{M}}{R_{\mathrm{NS}}}\,, \tag{2.4}$$

where M_{NS} and R_{NS} are the mass and radius of the neutron star, respectively. L can also be used to classify accretion regimes, as Eq. (2.4) only depends on $\dot{M}$ and constants. The physics of the accretion regimes is described in detail by Becker et al. (2012). In the following, I give a brief summary of the most relevant points.

For high accretion rates ($\dot{M} \gtrsim 10^{17}\,\mathrm{g\,s^{-1}}$), the radiative pressure is sufficient to stop the flow of infalling matter. This results in the formation of a radiative shock and an accretion column, which rises up from the surface. At $\dot{M} \lesssim 10^{16}\,\mathrm{g\,s^{-1}}$, the radiative pressure is not sufficient to bring the matter to rest. Instead, the matter is mainly stopped through Coulomb collisions. At even lower $\dot{M}$, the existence of a gas mediated shock is possible (Langer & Rappaport 1982). Particles reaching the surface can form a thermal mound, which is in thermal equilibrium with the neutron star's atmosphere, emitting blackbody radiation according to its temperature. If $\dot{M}$ decreases below $\sim 10^{15}\,\mathrm{g\,s^{-1}}$,

the accretion column disappears along with the shock. Instead, a hot spot forms, as the plasma particles are stopped in the atmosphere of the neutron star by Coulomb collisions. Accretions columns show distinct and complex behavior in the regimes described above. As hot spots are the main interest of this thesis, please refer to Becker et al. (2012) for further details.

Three mechanisms are responsible for the emission of X-rays (Becker & Wolff 2007). 1) Non-thermal bremsstrahlung, which is due to the deflection of infalling charged particles in the ambient plasma. 2) Blackbody radiation emitted by the thermal mound or thermalized layers of the atmosphere. 3) Cyclotron radiation, which is monochromatic and is caused by electrons being collisionally excited onto higher Landau levels (see Sect. 2.1.2) and which then de-excite radiatively. Note that the lifetime of an excited state is 10^{-15} s, which is much shorter than the time for collisional de-excitation. As the accreting matter reaches velocities of 0.6 c, the emitted bremsstrahlung is in the X-ray energy range. In addition, these high velocities cause the thermal mound to reach temperatures of up to 10^8 K, i.e., the blackbody photons are also in the X-ray energy range. The wavelength of Cyclotron radiation depends on the magnetic field strength and is in the X-ray range for $B = 10^{11}$–10^{13} G (see Eq. (2.3)). In the accretion column regime, bremsstrahlung is the dominant emission process (Becker & Wolff 2007). If no column is present, the main contribution comes from blackbody radiation.

2.2.2 Scattering and Spectrum

The X-ray photons created in the accretion process close to the neutron star's surface interact with the surrounding plasma before they escape from the emission region. For a full description, a radiative transfer equation has to be solved (Mihalas 1978). The scattering processes are mainly responsible for the shape of the spectrum of the escaping photons.

Of main importance is magnetic Compton scattering (see Sect. 2.1.2), which affects the radiation in the form of Bulk and Thermal Comptonization (Becker & Wolff 2007). In the former process, photons scatter on electrons in the accreting matter and decelerate it. Note that electrons and protons are coupled via Coulomb interaction and therefore, protons in the accreting matter are decelerated as well. This deceleration drives the formation of a radiative shock in the high-mass accretion regime. Thermal Comptonization is (inverse) Compton scattering on thermal electrons of the atmosphere.

In the high-mass accretion regime, these scattering processes provide an ansatz to explain the observed spectral shape (Becker & Wolff 2007), which is described by a power law with an exponential cutoff. The power law component is mainly attributed to Bulk Comptonization, while the energy transfer by thermal Comptonization leads to a high-energy exponential cutoff (Becker & Wolff 2007). Sometimes CRSFs are observed, usually above 20 keV (see Sect. 2.1.2). Recent observations of GX 304−1 (Tsygankov et al. 2019b) and A 0535+262 (Tsygankov et al. 2019a) in states of lower accretion rate revealed a different spectral shape with two humps. Figure 2.3 shows the spectrum of GX 304-1

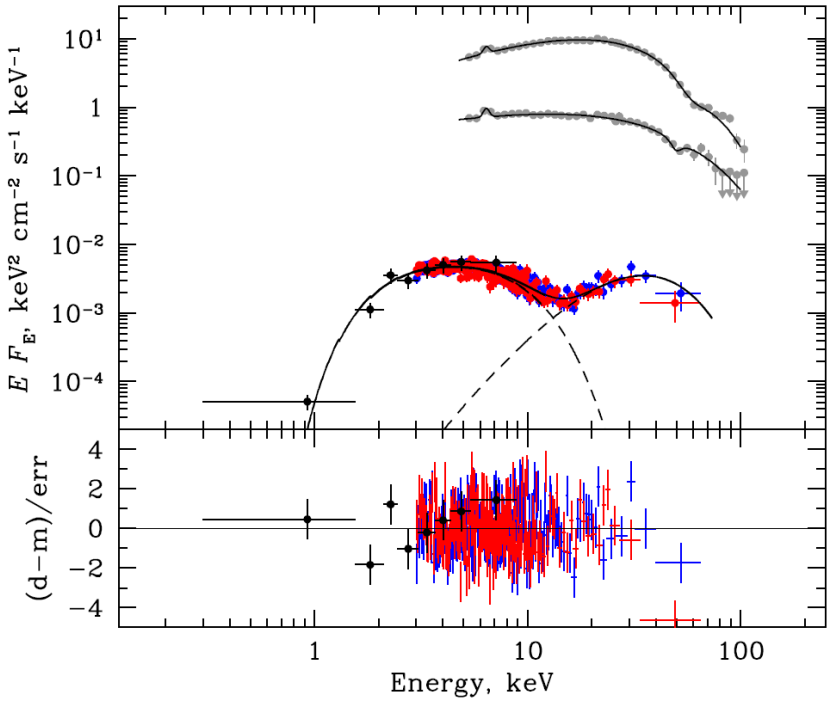

Figure 2.3: Spectra of GX 304-1 taken in states with different luminosities (Tsygankov et al. 2019b, Fig. 1). The upper two spectra (gray data points) follow the shape attributed to a high-mass accretion regime with an accretion column. The shape of the lower spectrum (red data points) deviates significantly, being composed of two broad humps.

and compares it to previous measurements at higher accretion rates. Tsygankov et al. (2019b) suggest that this change is related to a change in the mechanism decelerating the accreting matter, as it would be the case for a transition between a column and a hot spot regime. However, the origin of especially the higher energy hump is under debate.

2.3 Light bending

The curvature of spacetime influences the trajectories of photons. This so-called gravitational light bending effect will be briefly introduced in the following. A detailed description can be found in Falkner (2012, 2018) and references therein.

Einstein's equations describe how momentum and energy (and thereby mass) affect the curvature of spacetime, or more precisely, the metric. The metric, $g_{\mu\nu}$, defines a dot product in curved spacetime and specifies how distances and angles are measured. One of the simplest solutions of Einstein's equations is the Schwarzschild metric, which is valid in vacuum and assumes spherical symmetry. The line element of the Schwarzschild metric in spherical coordinates (t, r, θ, ϕ) is given by (e.g. Falkner 2012)

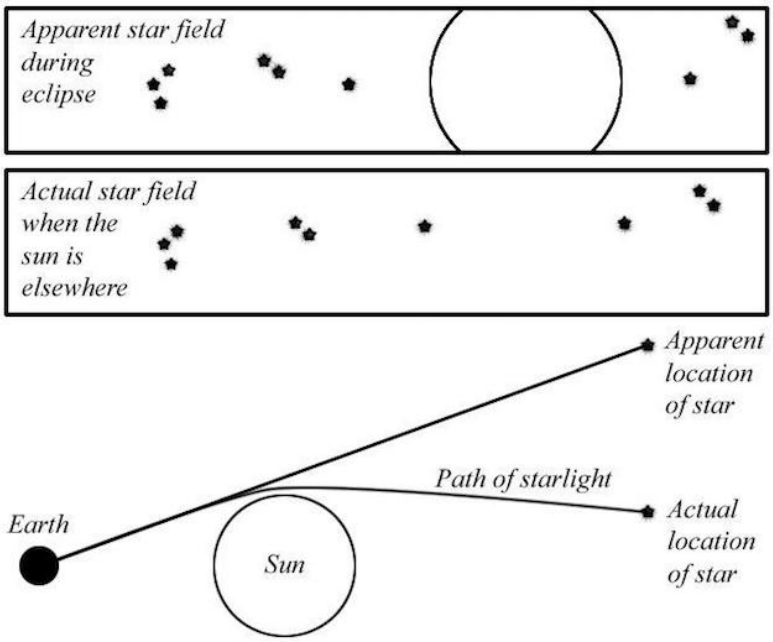

Figure 2.4: The sun's gravity bends the path of starlight and thereby changes the apparent location of a star. This effect can be observed during an eclipse. Credit: `http://cosmictimes.gsfc.nasa.gov`.

$$\mathrm{d}s^2 = -\left(1 - \frac{2M}{r}\right)\mathrm{d}t^2 + \left(1 - \frac{2M}{r}\right)^{-1}\mathrm{d}r^2 + r^2\left(\mathrm{d}\theta^2 + \sin\theta\,\mathrm{d}\phi^2\right)\,, \tag{2.5}$$

where M is the gravitating object's mass. The line element is related to the metric by

$$\mathrm{d}s^2 = g_{\mu\nu}x^\mu x^\nu. \tag{2.6}$$

In classical physics, free particles move on straight lines. This notion has to be expanded in general relativity. A geodesic is the shortest connection between two points in curved spacetime, i.e., the generalization of a straight line. As an example, imagine taking a flight from Europe to the US. On Earth, the shortest connection between two points lies on a great circle, which is a circle dividing the Earth in two equally sized hemispheres. The flight path will follow a great circle and therefore pass by Greenland, taking the plane further north than one would intuitively expect from standard map projections. Due to the principle of least action, particles travel along geodesics in curved spacetime. The trajectory of a particle is obtained by solving the Geodesic equation (e.g. Falkner 2012)

$$\frac{\mathrm{d}^2x^\lambda}{\mathrm{d}t^2} + \Gamma^\lambda_{\mu\nu}\frac{\mathrm{d}x^\mu}{\mathrm{d}t}\frac{\mathrm{d}x^\nu}{\mathrm{d}t} = 0\,, \tag{2.7}$$

where $\Gamma^{\lambda}_{\mu\nu}$ are the Christoffel symbols, which depend on the metric and its derivations. This result is also true for massless particles like photons and thereby gives rise to gravitational lensing and light bending effects. A common example is the apparent change of a star's position close to the sun (see Fig. 2.4). Likewise, X-rays created on the surface of a neutron star experience a light bending effect, which has to be taken into account when interpreting pulse profiles. In this case, the light bending only depends on the mass, M, of the neutron star and the radius, r, at which the light is emitted.

3 Parameters and Characteristics of the models

To describe emission from X-ray pulsars at low accretion rates, processes in the neutron star's atmosphere and relativistic light bending have to be modeled. In this chapter, the `polcap` model and the `LIBANS` code, which are used for the modeling of pulse profiles in chapter 4, are introduced.

3.1 The `polcap` model

At low accretion rates ($\dot{M} \lesssim 10^{15}\,\mathrm{g\,s^{-1}}$), no accretion column forms and the matter is mainly stopped by Coulomb collisions in the atmosphere, as discussed in Sect. 2.2.1. The `polcap` model (Sokolova-Lapa et al. 2019, in prep.) describes the transport of X-ray photons trough the atmosphere of the neutron star in this regime. Following Sokolova-Lapa et al. (2019, in prep.), the `polcap` model will be briefly introduced, before the resulting spectrum (see Sect. 3.1.1) and the emission profiles (see Sect. 3.1.2) are discussed.

The `polcap` model considers a plane parallel neutron star atmosphere with a column depth y_0, at the bottom of which blackbody photons are emitted according to a temperature kT_{BB}. This assumption is based on the fact that blackbody radiation from thermalized layers of the atmosphere is the main X-ray emission mechanism at low accretion rates (see Sect. 2.2.1). The column depth is defined as the integral of the density over the height of the atmosphere. Further parameters of the model are the radius of the emission region, r_0, the mass accretion rate, $\dot{M}$, and the magnetic field strength at the surface of the neutron star, which is specified in terms of the cyclotron energy, E_{cyc} (see Sect. 2.1.2). All five parameters are summarized in Fig. 3.1 and can currently be varied in the ranges shown in Tab. 3.1.

$\dot{M}$	$1\text{–}10 \cdot 10^{14}\,\mathrm{g\,s^{-1}}$
r_0	200–300 m
y_0	$6\text{–}9\,\mathrm{cm^{-2}\,g}$
E_{cyc}	63–71 keV
kT_{BB}	0.8–1.2 keV

Table 3.1: Parameter ranges of the `polcap` model.

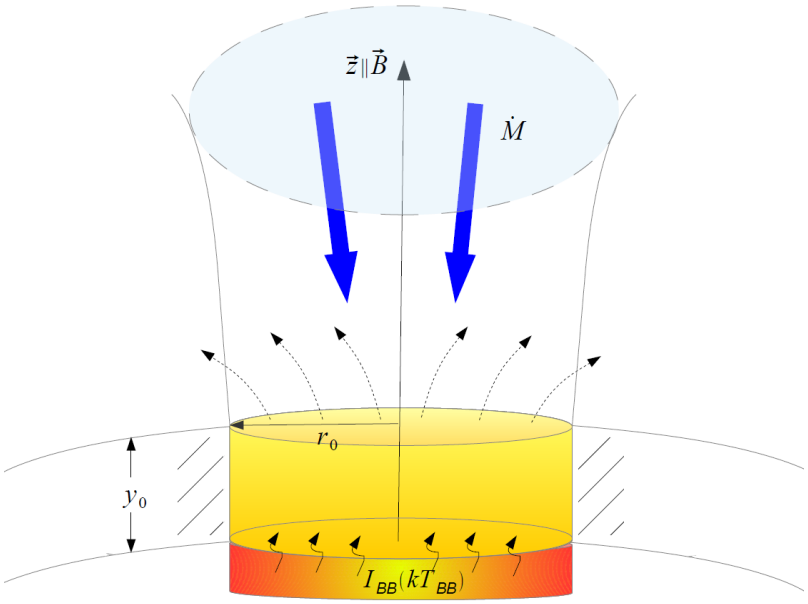

Figure 3.1: The five parameters of the `polcap` model (Sokolova-Lapa et al. 2019, Fig. 1): Accretion rate, $\dot{M}$, radius of the emission region, r_0, column depth, y_0, blackbody photon temperature, kT_{BB}, and magnetic field strength, B, which is given in terms of the cyclotron energy, E_{cyc}, in the model.

The ultimate goal of the model is to solve the equations of polarized radiative transfer for the blackbody photons originating on the neutron star's surface to obtain the spectral and angular distribution of photons escaping the emission region. Radiative transfer refers to scattering, absorption, and emission processes, which act on the blackbody photons. In polarized radiative transfer, the ordinary and extraordinary polarization modes (see Sect. 2.1.1) are treated separately. However, the modes are coupled due to scattering processes. The `polcap` model assumes pure vacuum normal modes, i.e., vacuum polarization is considered but not the effect of birefringent plasma (see Sect. 2.1.1).

Radiative transfer depends on the temperature and electron density profiles of the atmosphere. These profiles are calculated considering heating and cooling of the atmosphere's electron gas. Heating and cooling refer to mechanisms by which the electrons in the atmosphere gain and loose energy, respectively. The `polcap` model considers heating due to Coulomb collisions with accreting protons and cooling due to inverse Compton scattering and bremsstrahlung. The atmosphere is assumed to be static, such that heating and cooling balance each other out. Then, the temperature and density profiles are calculated based on the energy balance and hydrostatic equations.

From the temperature and electron density profiles, the cross sections of scattering, absorption and emission of blackbody photons in the atmosphere can be calculated. The `polcap` model takes into account Compton and inverse Compton scattering, as well as absorption due to bremsstrahlung. Due to the strong magnetic field and the resulting

Landau quantization, the cross sections of these processes are modified (see Sect. 2.1.2) to what is called magnetic Compton scattering and magnetic bremsstrahlung. The spectral and angular photon distributions resulting from these processes are discussed in the following sections.

3.1.1 Spectrum

In Sect. 2.2.2, the effect of magnetic Compton scattering on the spectrum was discussed for high accretion rates. The double hump shape measured in the case of low accretion rates was also introduced. In the following, the predictions from the polcap model for this low-mass accretion regime are discussed, following Sokolova-Lapa et al. (2019, in prep.).

Figure 3.2 shows the spectrum modeled by the polcap model, for a fixed set of parameters: $\dot{M} = 10^{14}\,g\,s^{-1}$, $E_{\rm cyc} = 88\,\mathrm{keV}$, $r_0 = 200\,\mathrm{m}$, and $kT_{\rm BB} = 1.4\,\mathrm{keV}$. The extraordinary and ordinary modes are given, as well as their sum. Note that energy flux multiplied with energy is shown. The spectrum consists of a broad hump at 1–10 keV and a second narrower peak. The beginning of a third peak above 100 keV is also visible.

Within the polcap model, this shape is explained as follows. The broad hump at 1–10 keV is mainly due to extraordinary thermal photons, for which the cross sections for magnetic Compton scattering and magnetic bremsstrahlung are low. The remaining two peaks result from a second hump, which is split in two by a cyclotron absorption line at $E_{\rm cyc} = 88\,\mathrm{keV}$. This split structure is often referred to as cyclotron wings. The second hump is a result of saturated Comptonization, i.e., the photons reach a thermodynamic equilibrium with the electrons of the atmosphere by magnetic Compton scattering.

The double hump shape predicted here is also seen in observations of X-ray pulsars at low accretion rates (see Fig. 2.3 in Sect. 2.2.2). From the explanation given above, the observed spectra are interpreted as follows. The lower hump is fully visible, while the second hump is cut at the cyclotron line energy. To summarize, the predicted spectrum fits the observations qualitatively. Further discussion and a fit to the data can be found in Sokolova-Lapa et al. (2019, in prep.).

3.1.2 Emission profiles

The emission profile specifies the intensity of radiation depending on the angle relative to the neutron star's surface, i.e., it contains information about the angular distribution of the escaping photons. Figure 3.3 shows emission profiles for the extraordinary (upper left), the ordinary (upper right), and the sum of both modes (bottom) in four energy bands (1–5 keV, 5–20 keV, 20–50 keV, 50–90 keV), as well as the sum of all bands. While the extraordinary mode is largely isotropic, the ordinary mode shows a wing structure with an additional central lobe. For both modes, the highest contribution to the overall intensity comes from the lowest energy band (1–5 keV). In the extraordinary mode, a deviation from the isotropic shape can be observed for the higher bands (20–50 keV and 50–90 keV).

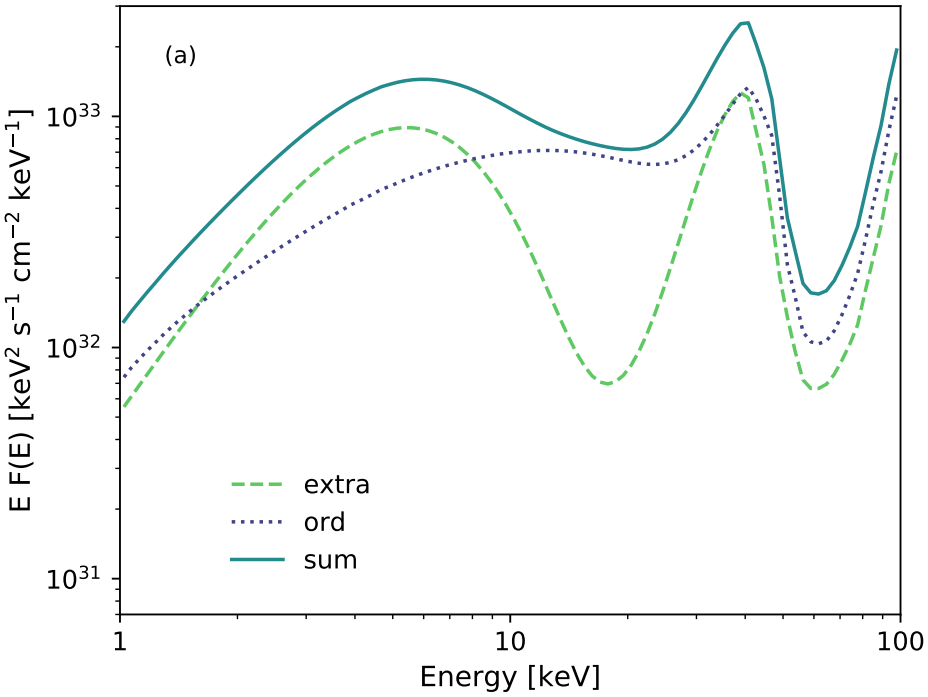

Figure 3.2: `polcap` spectrum for $\dot{M} = 10^{14}\,g\,s^{-1}$, $E_{\mathrm{cyc}} = 88\,\mathrm{keV}$, $r_0 = 200\,\mathrm{m}$, and $kT_{\mathrm{BB}} = 1.4\,\mathrm{keV}$. The extraordinary mode is indicated by the dashed line, the ordinary mode by the dotted line, and the sum of both modes by the solid line. On the y-axis, energy flux multiplied by energy is given.

For lower energies, a higher flux is predicted by the `polcap` model (see Sect. 3.1.1), which explains the domination of the 1–5 keV band. Note that the spectrum in Fig. 3.2 is multiplied by the energy, such that the energy emitted per energy decade is shown. As a result, the contribution from higher energies appears larger. The isotropic behavior of the extraordinary mode is due to low cross sections for magnetic Compton scattering in magnetic bremsstrahlung (see Sect. 3.1.1). At higher energies, the emission profile is shaped by the directional dependence of these cross sections, which is due to the formation of quantized Landau levels in high magnetic fields (see Sect. 2.1.2). This directional dependence is also responsible for the wing shape of the ordinary mode (Sokolova-Lapa et al. 2019, in prep.).

Emission profiles provide a key in the interpretation of pulse profiles, as the observer's viewing angle on the hot spot changes in the course of rotation. Of equivalent importance is light bending, which is implemented by the code introduced in the following chapter. A detailed discussion of the interpretation of pulse profiles follows in Sect. 4.1.

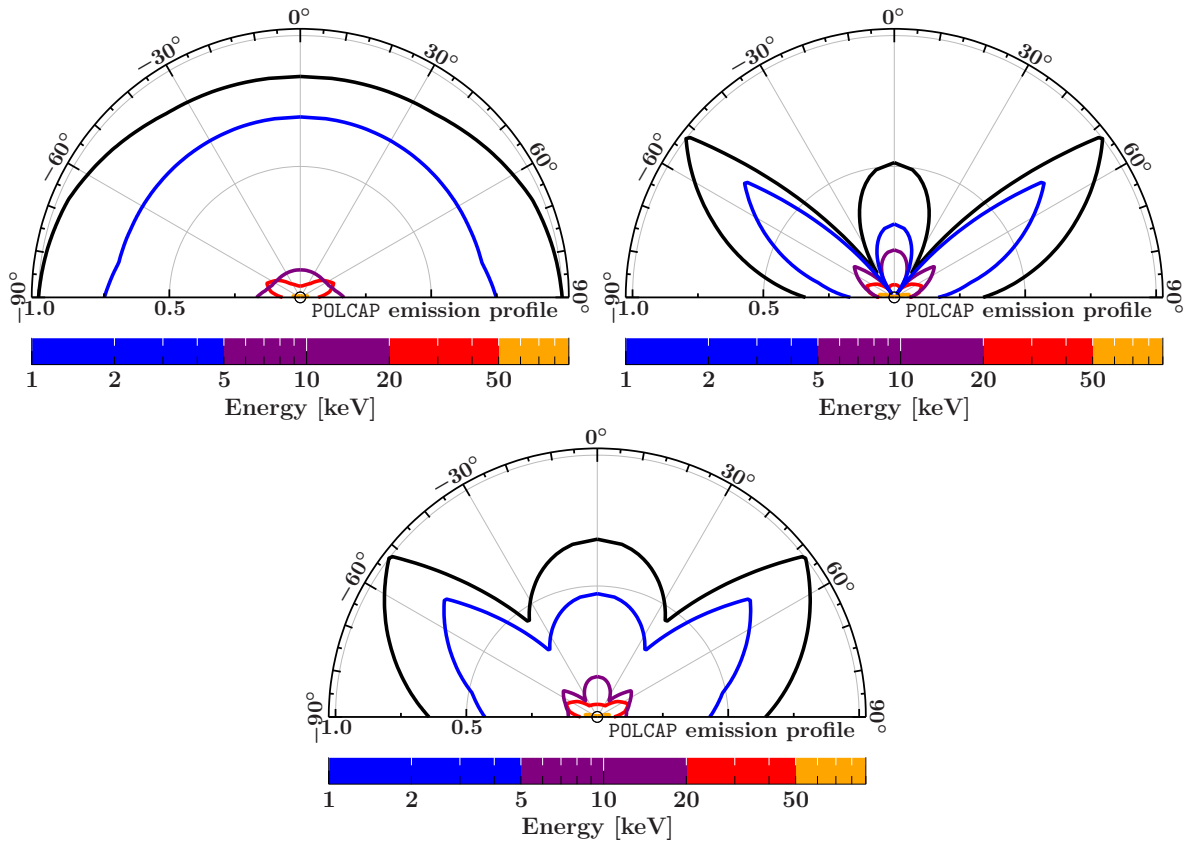

Figure 3.3: Emission profile of the `polcap` model for the extraordinary (upper left), ordinary (upper right), and combined modes (bottom). The shape of the emission profile in different energy bands is shown in color. The black line indicates the sum of all bands. The intensity of the radiation is shown, normalized to its maximal value.

3.2 The LIBANS code

Particles move along geodesics in curved spacetime, as explained in Sect. 2.3 of Chapter 2. The `LIBANS` (LIght Bending around Accreting Neutron Stars) code (Falkner 2012, 2018) models the trajectories of photons emitted by an accretion column or hot spot on the surface of a neutron star. The code yields the flux depending on the pulse phase, i.e., the pulse profile. Different emission models can be chosen. Here, the main aspects of the model will be briefly introduced. In Chapter 4, the `LIBANS` code is combined with the `polcap` model. This section summarizes the main aspects of the `LIBANS` code, following Falkner (2012, 2018).

The core of the `LIBANS` code is the projection of the neutron stars surface onto the observer sky. Without light bending, the observer would see the hot spot under an angle Ψ, which is called the apparent emission angle. Ψ is given by

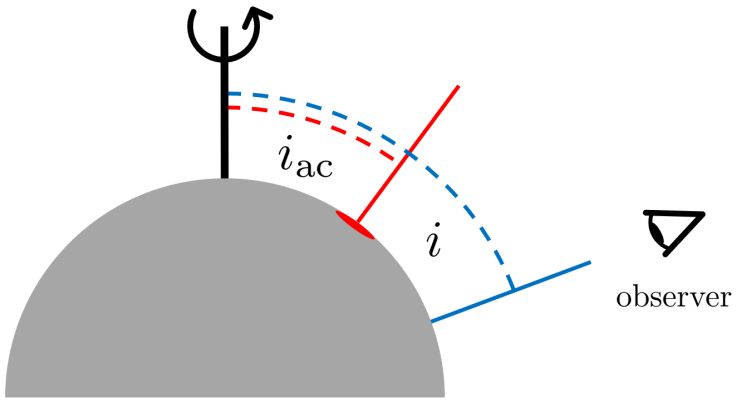

Figure 3.4: Visualization of the definition of observer inclination, i, (shown in blue) and inclination of the hot spot, i_{ac}, (shown in red).

$$\cos\Psi(\phi) = \cos i \cos i_{\mathrm{ac}} + \sin i \sin i_{\mathrm{ac}} \cos\phi\,, \tag{3.1}$$

where i is the observer inclination, i_{ac} is the inclination of the hot spot, and ϕ is the phase angle of the neutron star. At $\phi = 0°$, the hot spot is seen from up front, whereas at $\phi = 180°$ it is directly on the opposite side, the farthest away from the observer. The angles i and i_{ac} are measured with respect to the rotational axis of the neutron star, as shown in Fig. 3.4.

Due to light bending, the remote observer does not see the hot spot under the angle Ψ, but under the light bent angle, η, which can be calculated by solving the Geodesic equation (Eq. (2.7)). The `LIBANS` code assumes a Schwarzschild metric (Eq. (2.5)) for a neutron star of mass M_{NS}. Unfortunately, the Geodesic equation is not analytically solvable in this case. Therefore, Falkner (2012, 2018) uses an analytic approximation introduced by Beloborodov (2002). The accuracy of the approximation is sufficient for the study of pulse profiles. In this approach, η is given by

$$\cos\eta(\phi) = 1 - (1 - \cos\Psi(\phi)) \left(1 - \frac{R_{\mathrm{S}}}{R_{\mathrm{NS}}}\right), \tag{3.2}$$

where $R_{\mathrm{S}} = 2GM_{\mathrm{NS}}/c^2$ is the Schwarzschild radius of the neutron star.

The `LIBANS` code performs the calculation in several steps. 1) The parameters are set. This includes physical parameters, such as the mass M_{NS} and radius R_{NS} of the neutron star, the geometric parameters i and i_{ac}, as well as parameters concerning the modeling. 2) The objects for the neutron star and the accretion columns or hot spots are created. The surface is modeled using a triangle mesh, as shown in Fig. 3.5. 3) Parameters of the trajectory are calculated for each surface element and stored in a lookup table. This calculation is followed by 4) an interpolation step and 5) the projection of the surface

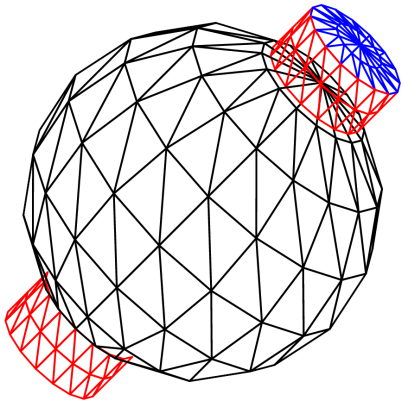

Figure 3.5: A neutron star with two accretion columns modeled by the LIBANS code (Falkner 2012, Fig. 3.4).

elements onto the observer sky, which is the core of the program. After 6) a correction for overlapping surface elements is performed, 7) the flux is calculated.

One of the main consequences of light bending is that parts of the surface are seen which are hidden in the geometric projection. Figure 3.6 compares the geometric to the relativistic projection. The neutron star appears visibly larger in the relativistic projection. The hot spot is fully visible, which is not the case in the geometric projection. In other words, photons emitted on the far side of the neutron star reach the observer in some cases. However, depending on the neutron star's mass and radius, there can be a region where no trajectory exists that reaches the observer. This region is called the shadow zone and is marked in red in Fig. 3.7. The trajectories of photons emitted on the neutron stars surface that reach the observer are shown in green.

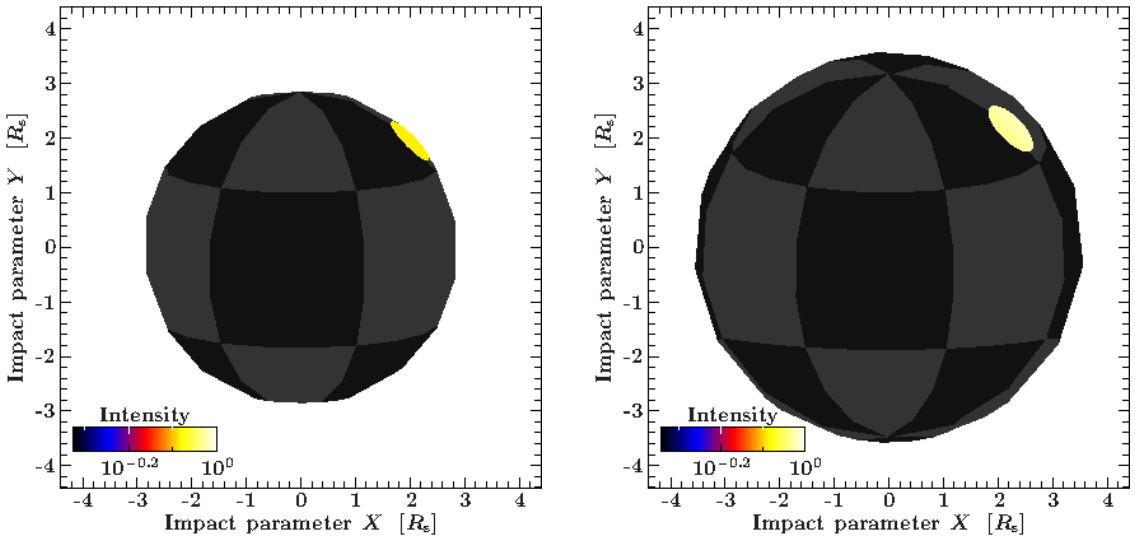

Figure 3.6: Comparison of the geometric (left panel) and relativistic (right panel) projection, for a neutron star of mass $M_{\mathrm{NS}} = 1.4\,M_{\odot}$, radius $R_{\mathrm{NS}} = 12\,\mathrm{km}$ and radius of the hot spot $r_{\mathrm{ac}} = 250\,\mathrm{m}$, with $i = 80°$, $i_{\mathrm{ac}} = 45°$ in phase $\phi = 78.75°$. The color of the hot spot indicates the X-ray intensity obtained by the `polcap` model, normalized to its maximal value. The size of the hot spot is enlarged by a factor of 8. The impact parameters in X and Y are given as a multiple of the Schwarzschild radius, R_{s}.

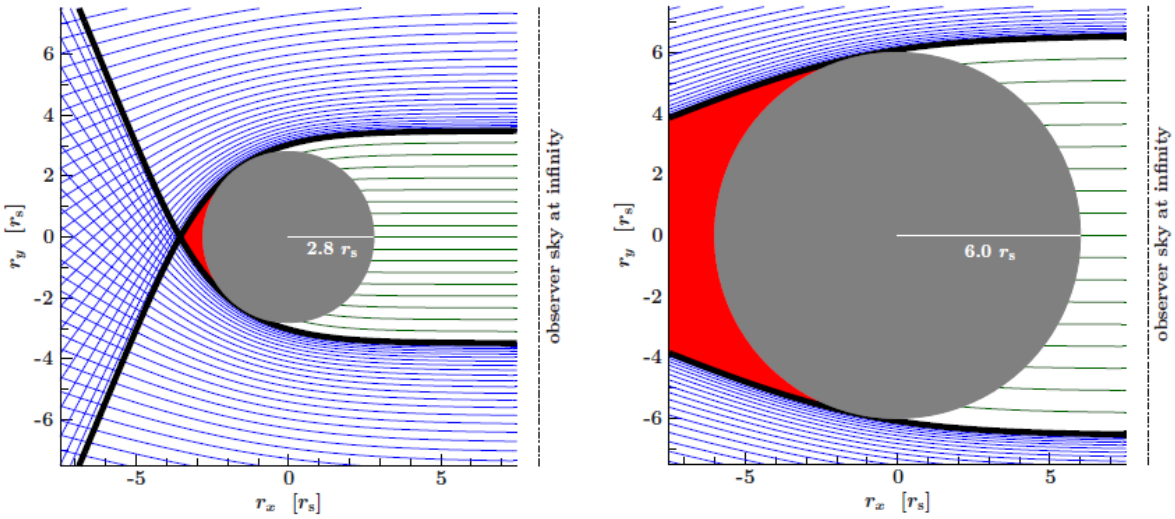

Figure 3.7: Photon trajectories (blue and green lines) for neutron stars with different radii (Falkner 2012, Fig. 3.9). The shadow zone is indicated in red. A detailed description can be found in Falkner (2012). r_x and r_y are the impact parameters in x and y, given in multiples of the Schwarzschild radius (indicated with r_{s} here).

4 Pulse profiles

To arrive at a model for pulse profiles of X-ray pulsars, both emission geometry and light bending have to be considered. The emission profile, i.e., the intensity of the radiation depending on the angle relative to the neutron star's surface (see Sect. 3.1.2), only accounts for what an observer in the system of the neutron star would see. The transformation to the system of the remote observer is done by applying the `LIBANS` code (Falkner 2012, 2018), which is described in Sect. 3.2. This chapter aims to combine the `LIBANS` code with the `polcap` (Sokolova-Lapa et al. 2019, in prep.) model, which is valid for low accretion rates ($\dot{M} \lesssim 10^{15}\,\mathrm{g\,s^{-1}}$), as discussed in Sect. 3.1.

Pulse profiles depend on several factors, as laid out in Sect. 1.2. Therefore, this analysis will be restricted to geometric parameters, i.e., to the inclination to the observer, i, and the inclination of the hot spot, i_{ac}. The change due to physical parameters of the `polcap` model is expected to be small within the range that is implemented in the model (see Sect. 3.1). I investigate a neutron star of mass $M_{\mathrm{NS}} = 1.4\,M_{\odot}$ and radius $R_{\mathrm{NS}} = 12\,\mathrm{km}$. For simplicity in the interpretation of the pulse profiles, a single hot spot of radius $r_0 = 250\,\mathrm{m}$ is considered. The accretion rate was set to $\dot{M} = 5 \cdot 10^{14}\,\mathrm{g\,s^{-1}}$, the seed photon temperature to $kT_{\mathrm{BB}} = 1\,\mathrm{keV}$, the column depth of the atmosphere to $y_0 = 7\,\mathrm{g\,cm^{-2}}$ and the cyclotron energy to $E_{\mathrm{cyc}} = 65\,\mathrm{keV}$. In addition, I investigate the ordinary and extraordinary polarization modes separately in Sect. 4.3 and 4.4. As their emission profiles differ, a clear dependence on the polarization is expected in the pulse profiles. In Sect. 4.2 and 4.3 a broad energy band from 1–90 keV is considered, whereas four distinct energy bands are investigated in Sect. 4.4 (1–5 keV, 5–20 keV, 20–50 keV, 50–90 keV). Throughout the analysis, all stated energy fluxes are normalized to their respective maximal values. The pulse profiles are sampled on 32 points in one pulse phase. This resolution is sufficient to investigate all structures that are seen in the pulse profiles.

4.1 Interpreting pulse profiles

For a fixed point in time, the hot spot is seen from a specific angle, which depends on i, i_{ac}, and the pulse phase. At a pulse phase of 0 (phase angle $\phi = 0°$), the hot spot is seen from up front, whereas at 0.5 ($\phi = 180°$) it is directly on the opposite side, the farthest away from the observer. An example for $i = 90°$ and $i_{\mathrm{ac}} = 45°$ is shown in Fig. 4.1. Note that the hot spot is extended and as a consequence, parts of its surface are seen under slightly different angles. As the emission profile is not isotropic, the intensity is not necessarily uniform over the full hot spot.

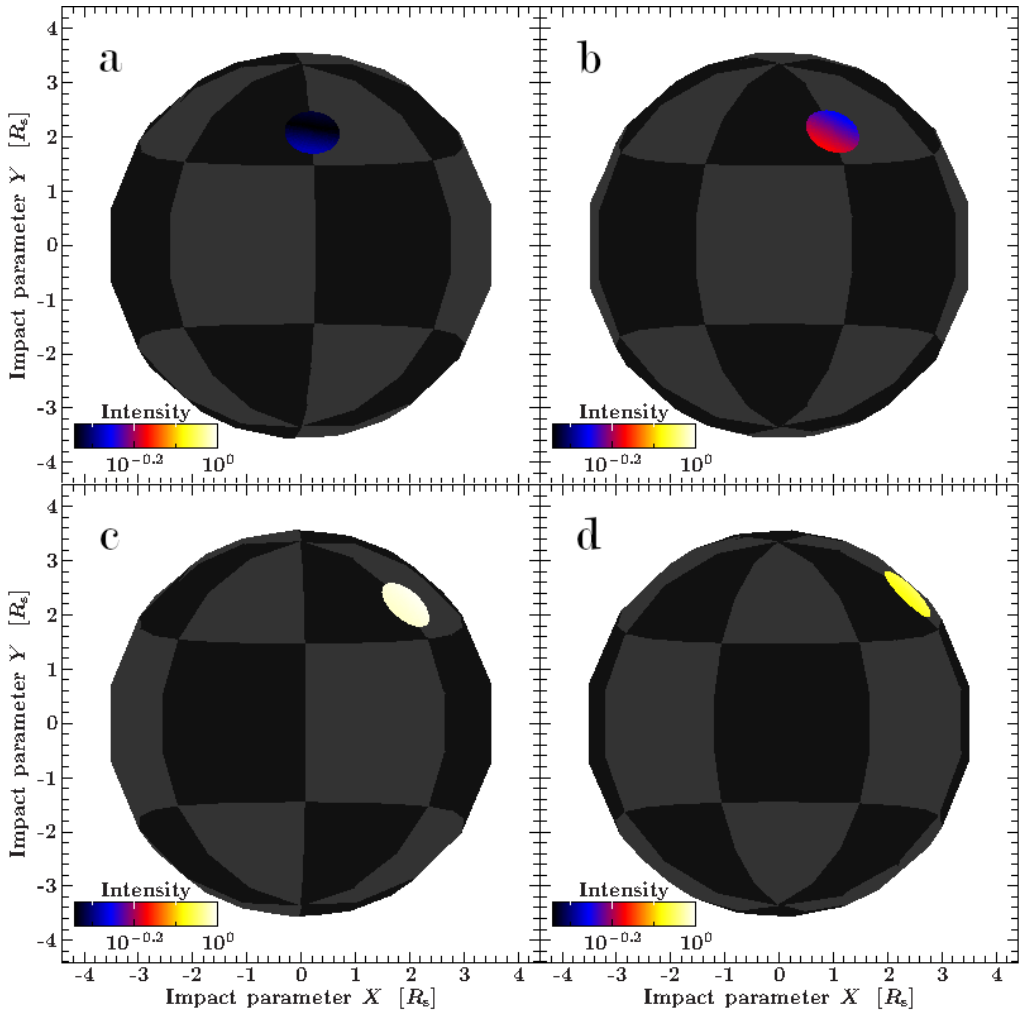

Figure 4.1: A neutron star with $i = 90°$, $i_{ac} = 45°$ in different phases of rotation as seen from the observer, i.e., light bending included. Panel **a** corresponds to a phase angle of 0°, **b** to 22.5°, **c** to 56.25°, and **d** to 90°. The hot spot is enlarged by a factor of 8 for better visibility. The color specifies the intensity. The impact parameter is given in multiples of the Schwarzschild radius R_s.

The emission profile specifies the flux that is emitted under each angle. In other words, a fixed combination of i, i_{ac}, and pulse phase corresponds to a viewing angle, from which the observer sees the emission profile. As the neutron star rotates, the pulse phase changes and thereby the viewing angle. For the phases shown in panels **a** to **d** of Fig. 4.1, the corresponding viewing angles are given in Fig. 4.2. In panel **a**, the hot spot shows a very low intensity, as the viewing angle happens to correspond to a minimum in the emission profile. With the rotation of the neutron star, the viewing angle gets larger and moves out of the minimum. Therefore, the intensity rises between panels **a** and **b**. This trend continues until the maximum is reached at **c**. From **c** to **d**, there is a slight decrease in the intensity, which is also seen in the emission profile.

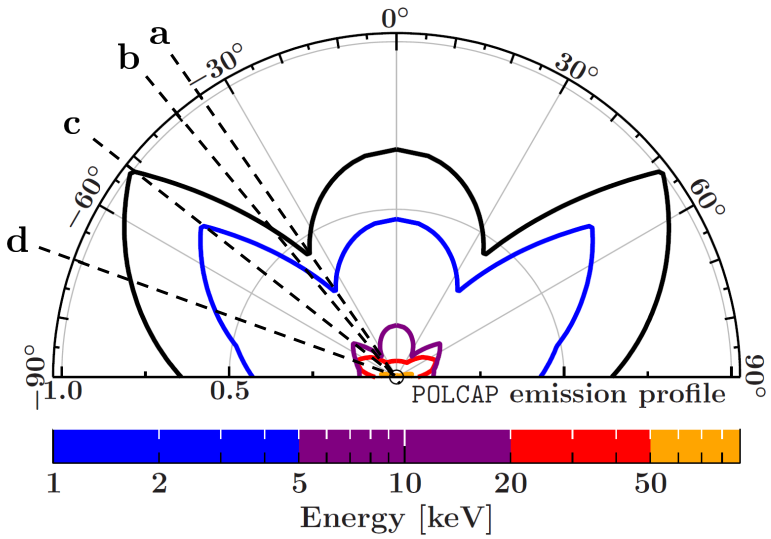

Figure 4.2: The emission profile for the sum of modes, as introduced in Sect. 3.1.2. Viewing angles corresponding to the rotation phases in Fig. 4.1 are indicated.

Note that the angles in Fig. 4.2 differ from what would be expected geometrically, e.g. in panel **a**, an angle of 45° would be expected, as the hot spot is inclined by 45° and the line of sight is perpendicular to the rotational axis. Instead, the remote observer's viewing angle is smaller, $\sim 36°$. This difference is due to light bending, which enlarges the visible surface area (see Fig. 3.6 in Sect. 3.2) and changes the observer's viewing angle on the hot spot. To obtain the correct angle, one has to transform from the system of the neutron star to the system of the observer, as described in Sect. 3.2 and specified by Eq. (3.2).

The shape of the emission profile causes the flux to change when the hot spot is observed from different angles. Note that there is an important difference between flux and intensity. The intensity is independent of the apparent area that the hot spot has for the observer, whereas the flux takes this into account. That is, the flux is given by the intensity integrated over the hot spot area, projected on the observers plane of view.

The pulse profile belonging to Fig. 4.1 is shown in Fig. 4.3. Here and in the following, two full pulse phases are plotted to better visualize the pulse profile's structure. Note that the pulse profile is mirrored at pulse phase 0.5, due to the symmetry of the emission profile. As expected from the emission profile, the highest flux is observed in phase **c**. However, the flux at **d** is lower than at **a** and **b**, even though the reverse is true for the intensities. This apparent contradiction is due to the effect of area projection discussed above. Point **d** corresponds to a rotation phase of 90°, i.e., the hot spot is seen from the side and therefore the projected area is small. In contrast, at **a** and **b**, the hot spot is seen directly or almost directly face on.

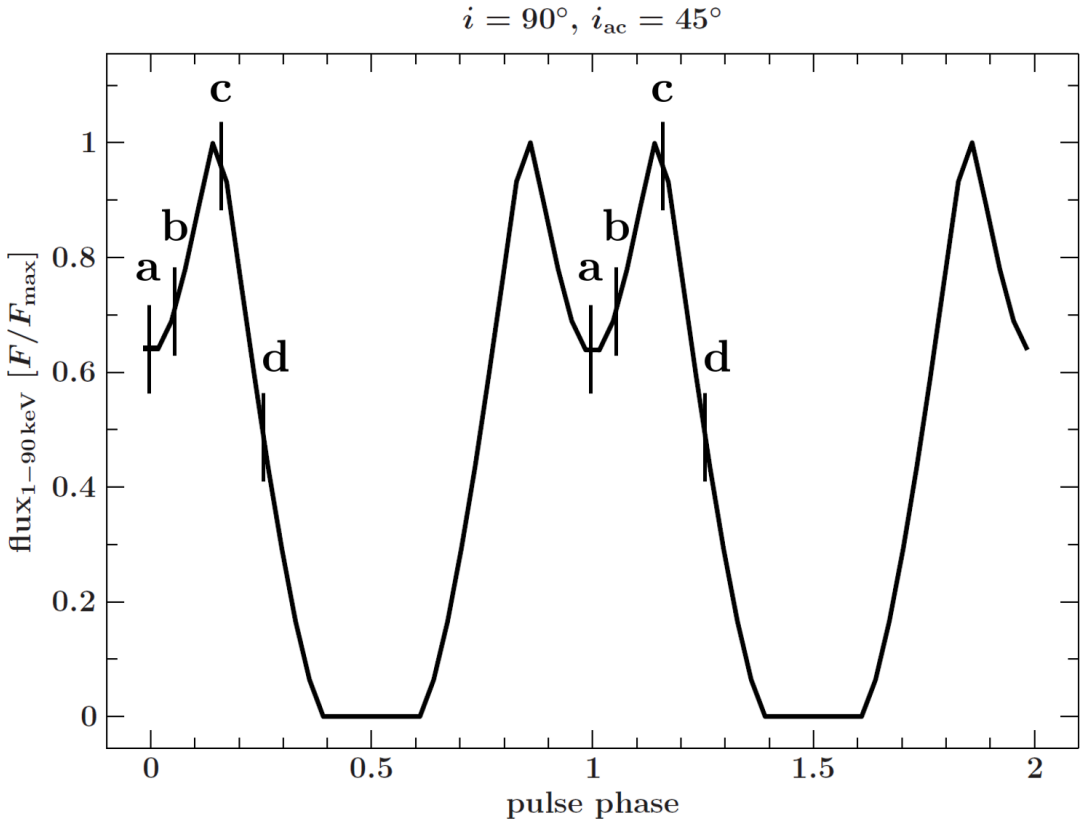

Figure 4.3: Pulse profile for a neutron star with $i = 90°$, $i_{ac} = 45°$. Energy flux is shown, normalized by its maximal value. The markers indicate pulse phases shown in Fig. 4.1, which also correspond to the viewing angles in Fig. 4.2.

To summarize, two factors are decisive for the interpretation of pulse profiles based on the emission profile. 1) Light bending changes the observer's viewing angle. 2) Flux is obtained from intensity, by taking into account the projected area of the hot spot. This understanding allows the interpretation of the pulse profiles in the following sections.

4.2 Geometric parameters: i, i_{ac}

To study how the pulse profiles depend on the geometric parameters i and i_{ac}, both parameters were separately varied over their full range, while leaving the energy range fixed at 1–90 keV and taking the sum of both polarization modes. The results are shown in Fig. 4.4 and 4.5. The parameters in these figures were chosen such that the resulting pulse profiles are representative for all possible shapes observed over the range of the varied parameter.

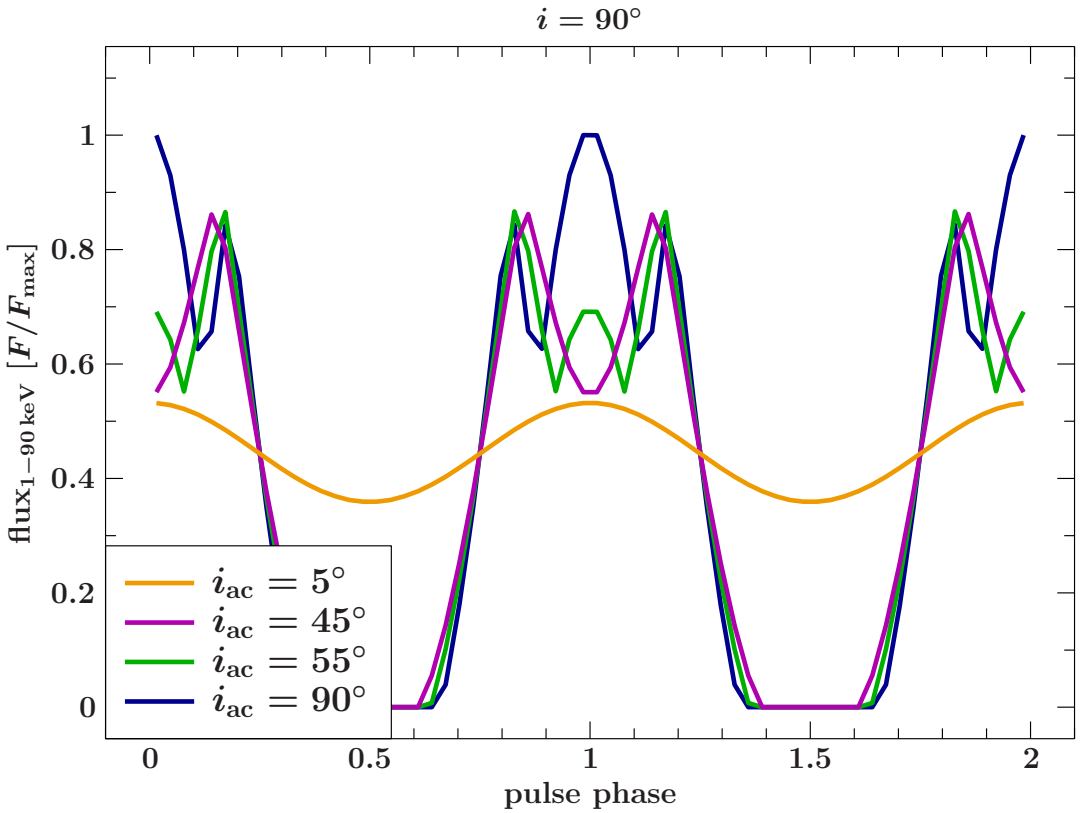

Figure 4.4: Pulse profiles for fixed $i = 90°$ and i_{ac} varying between 5° and 90°. The physical parameters are as described in the beginning of this chapter.

In Fig. 4.4, i_{ac} is varied while $i = 90°$ is fixed, i.e., the line of sight is perpendicular to the rotational axis. For small i_{ac}, the pulse profile is sinusoidal. As i_{ac} rises, its amplitude grows and a minimum appears at pulse phase 0. At $i_{\mathrm{ac}} = 55°$, this minimum has split in two, making room for an emerging maximum, which grows into a global maximum.

For low i_{ac}, the hot spot is close to the rotational axis, moving little as the neutron star rotates. Therefore, the angle under which it is seen only changes slightly, which explains the small variation in flux. The sinusoidal shape is mostly due to the area projection effect discussed in the previous section. In the edge case of $i_{\mathrm{ac}} = 0°$ the pulse profile is flat, because there is no change in the position of the hot spot relative to the observer. This result is true, independent of the value of i.

As i_{ac} rises, the inner parts of the emission profile become visible. At $i_{\mathrm{ac}} = 45°$, the minimum of the emission profile is seen, which explains the drop in the emission profile at pulse phase 0, as described in the previous section. For even larger i_{ac}, radiation from the central lobe reaches the observer. This causes a maximum to arise inside the minimum at phase 0. The area projection effect supports this and is responsible for the steepening of the pulse profiles around pulse phase 0.25. During phases with zero flux, the hot spot

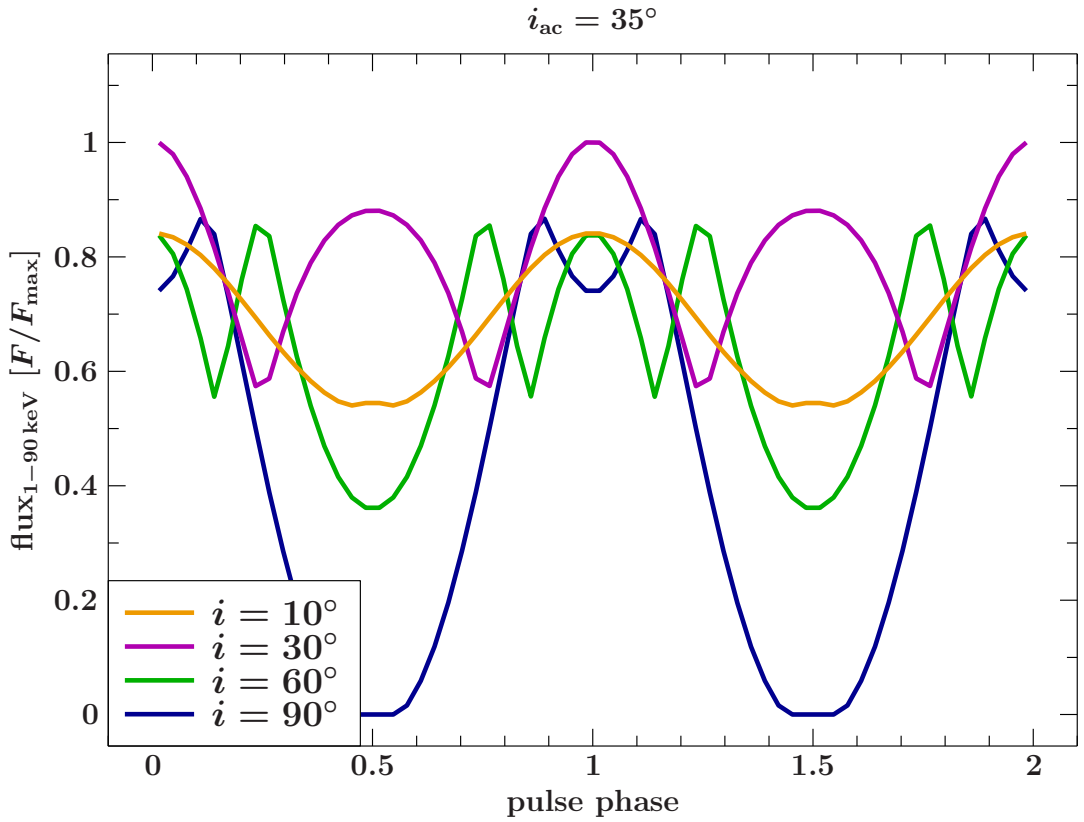

Figure 4.5: Pulse profiles for fixed $i_{ac} = 35°$ and varying i between 10° and 90°. The physical parameters are as described in the beginning of this chapter.

is in the shadow zone of the neutron star and therefore invisible for the observer.

In contrast to Fig. 4.4, $i_{ac} = 35°$ is fixed and i is varied in Fig. 4.5. The observer is therefore looking at a hot spot inclined by $i_{ac} = 35°$ from different directions. Similar to before, a sinusoidal shape is observed for small i. With rising i, a maximum emerges at pulse phase 0.5, splitting the minimum in two, as seen for $i = 30°$. On further increase, this maximum splits also, leaving behind a minimum which deepens, until the flux is zero at phase 0.5 for $i = 90°$.

In order to understand why the variation of flux is smaller for smaller i, imagine an observer that looks directly on the rotational axis, i.e., $i = 0°$. As the neutron star rotates, the position of the hot spot changes, possibly largely, depending on i_{ac}. However, the observer always sees the hot spot under the same angle, because the angle of the hot spot with respect to the rotational axis is fixed. Therefore, the observed flux is constant over time. Similarly, a small i leads to a small variation in the flux.

At $i = 30°$, the observers inclination is similar to the inclination of the hot spot. Hence, the observer sees the hot spot almost directly from the top at phase 0, which explains the global maximum present there. The second maximum at phase 0.5 comes from the wings of the emission profile. For $i \lesssim 30°$, this maximum gets smaller, as the wings cannot be

fully seen. This decrease continues until, at $i = 10°$, only a small kink is visible in the pulse profile, which allows the conclusion that below 10°, only the central lobe is visible.

With growing i the viewing angle gets larger, because the observer sees the hot spot more from the side and less from the top. For $i = 60°$, a minimum occurs at pulse phase 0.5, because of the intensity drop above a viewing angle of $\sim 55°$ in the emission profile. This minimum deepens as i grows further, while the maximum at phase 1 disappears, as the central lobe is not visible for viewing angles $\lesssim 35°$. A similar situation arose for $i = 90°$ and $i_{\mathrm{ac}} = 45°$ in the previous discussion concerning Fig. 4.4.

In conclusion, variation of the geometric parameters alone leads to a large variety of pulse profiles. In some cases, a change of 10°–20° causes the profile to change drastically (e.g. between $i = 10°$ and $i = 30°$ in Fig. 4.5). Up to three maxima and minima can arise in one pulse phase, depending on the covered range of viewing angles for chosen i and i_{ac}. A full interpretation of the pulse profiles can be reached when the structure of the emission profile, light bending, and area projection are considered.

4.3 Polarization

In strong magnetic fields, the ordinary and extraordinary polarization modes have different scattering cross sections, as discussed in section 2.1.1. This leads to a large difference in their emission profiles. While the emission profile is largely isotropic for the extraordinary mode, a pronounced wing structure dominates for the ordinary mode (see Fig. 3.3 in chapter 3). This difference becomes apparent, when investigating the pulse profiles for both modes separately.

In Fig. 4.6 and 4.7, i and i_{ac} are varied in the same way as in Fig. 4.4 and 4.5, with fixed parameters $i = 90°$ and $i_{\mathrm{ac}} = 35°$, respectively. It can be observed that all structure seen in the sum of modes is due to the ordinary mode. An exception is the increase at phase 0 and decrease at 0.5, which comes from the sinusoidal pulse profile of the extraordinary mode.

As before, these shapes are explained by the respective emission profiles for both modes, in combination with light bending and the area projection effect. For the extraordinary mode, the emission profile is largely isotropic. Therefore, the pulse profiles shape is goverend by the area projection effect, which leads to a sinusoidal shape. The flat minima are caused by the hot spot being in the shadow zone. For the ordinary mode, the discussion from the previous chapter holds up, as the emission profile has the same shape as the one for the sum of modes, only with more pronounced features.

In conclusion, pulse profiles from the extraordinary and ordinary modes differ greatly, due to their scattering behavior. Understanding how each mode contributes to an observed pulse profile is therefore crucial to explain the observations. In turn, measuring polarization and disentangling the components can help in constraining the geometry of the emission region.

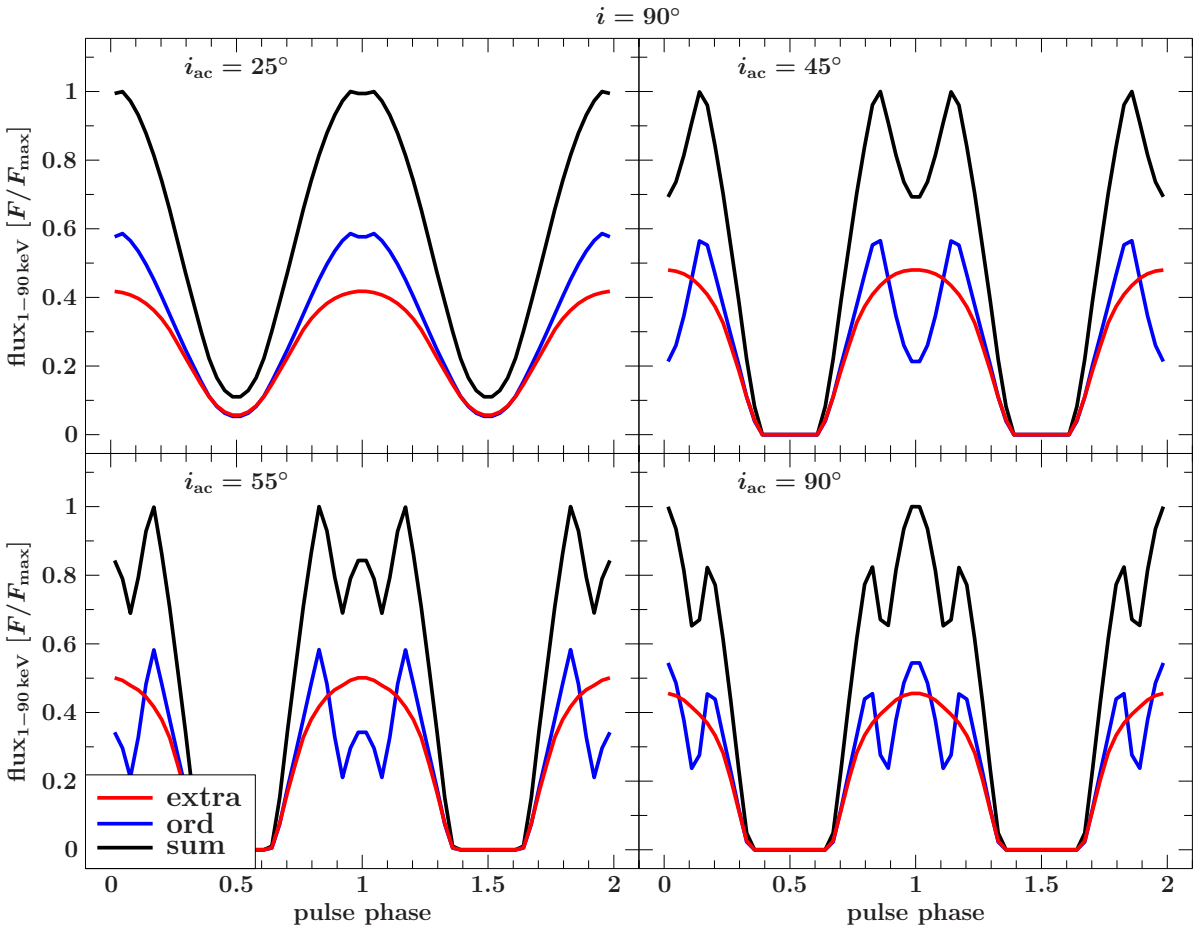

Figure 4.6: Pulse profile for the extraordinary (red), the ordinary (blue) and the sum (black) of both modes. $i = 90°$ is fixed while i_{ac} is varied between 25° and 90°. The physical parameters are as described in the beginning of this chapter.

4.4 Energy

In addition to the variation of geometric parameters and the polarization modes, the energy dependence of the pulse profiles is investigated in this section. Four bands were chosen: 1–5 keV, 5–20 keV, 20–50 keV, and 50–90 keV. As discussed in Sect. 3.1.2, most radiation is emitted in the 1–5 keV band. Therefore, this band will mostly shape the broad band pulse profiles discussed in the previous sections. The cyclotron line is contained in the 50–90 keV band, which causes the emission profile to change, as discussed in Sect. 3.1.2.

An exemplary $i_{ac} = 35°$ was chosen, with $i = 90°$ (Fig. 4.8) and $i = 60°$ (Fig. 4.9). Both combinations were discussed in the previous sections, with respect to the broad energy band. The pulse profile for $i_{ac} = 35°$, $i = 90°$ shows one maximum in half a pulse phase, which is due to the wings of the emission profile. The case of $i_{ac} = 35°$, $i = 60°$ shows two, which is the maximal number possible, as both wings and central lobe are visible.

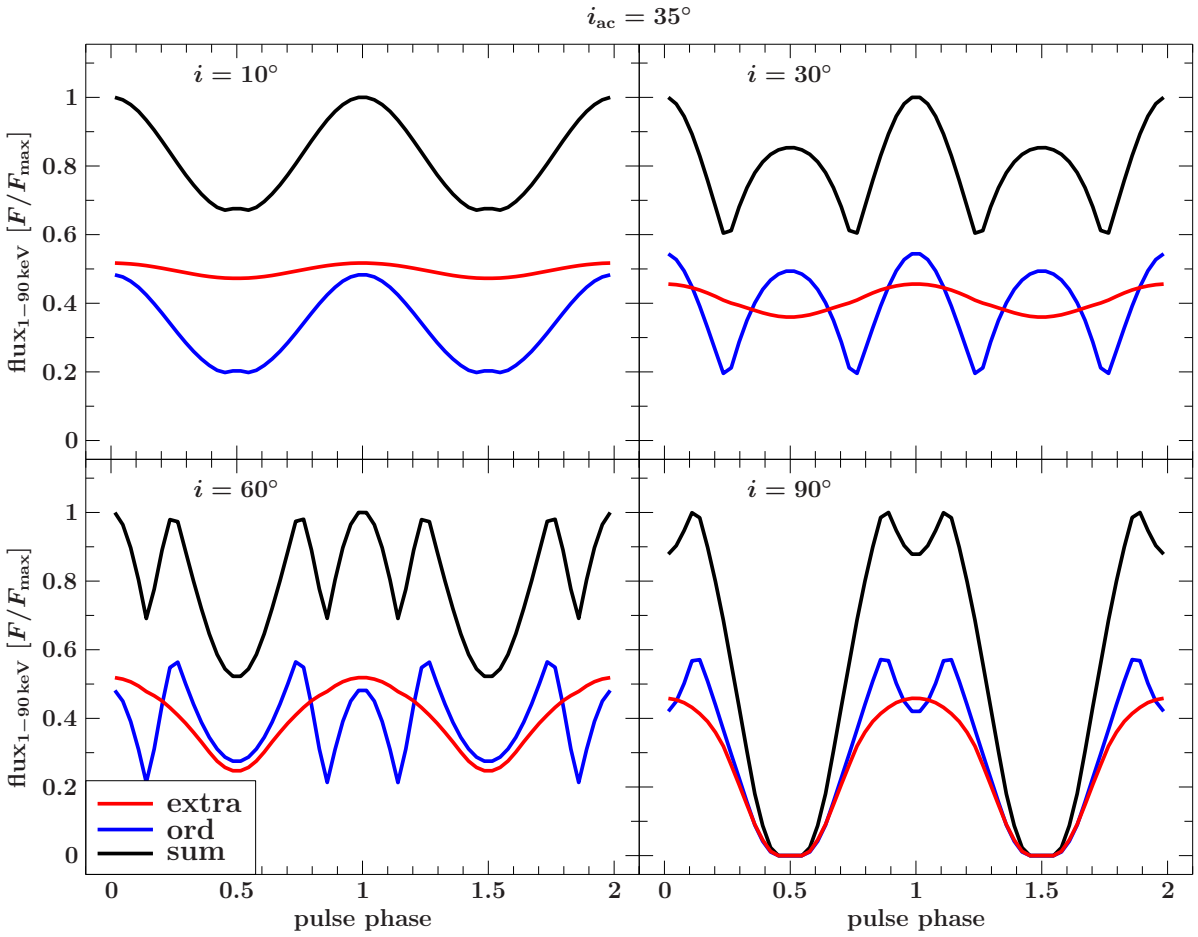

Figure 4.7: Pulse profile for the extraordinary (red), the ordinary (blue) and the sum (black) of both modes. $i_{ac} = 35°$ is fixed while i is varied between 10° and 90°. The physical parameters are as described in the beginning of this chapter.

This quantitative difference motivates the choice of parameters.

In Fig. 4.8, the shape of the pulse profiles stays mostly unchanged over all energy bands, except for the highest one. There, the extraordinary mode shows two small maxima, compared to one in the lower bands. The same is true in Fig. 4.9, but here the change is more pronounced. In both figures, the maxima and minima in the highest energy band are smoother than in the lower bands. For $i_{ac} = 35°$, $i = 60°$, the 50–90 keV band shows less variability in flux than the lower bands. All in all, the main difference between the energy bands is the change in heights of minima and maxima, as seen, e.g., by comparing bands 1 to 3 in Fig. 4.9. In contrast, the pulse phase at which minima and maxima are found is mostly unchanged. However, small shifts are seen in the highest energy band containing the cyclotron line.

As discussed in Sect. 3.1.2, the emission profile for the extraordinary mode shows a wing structure in the 50–90 keV band. In the other energy bands, emission from this mode

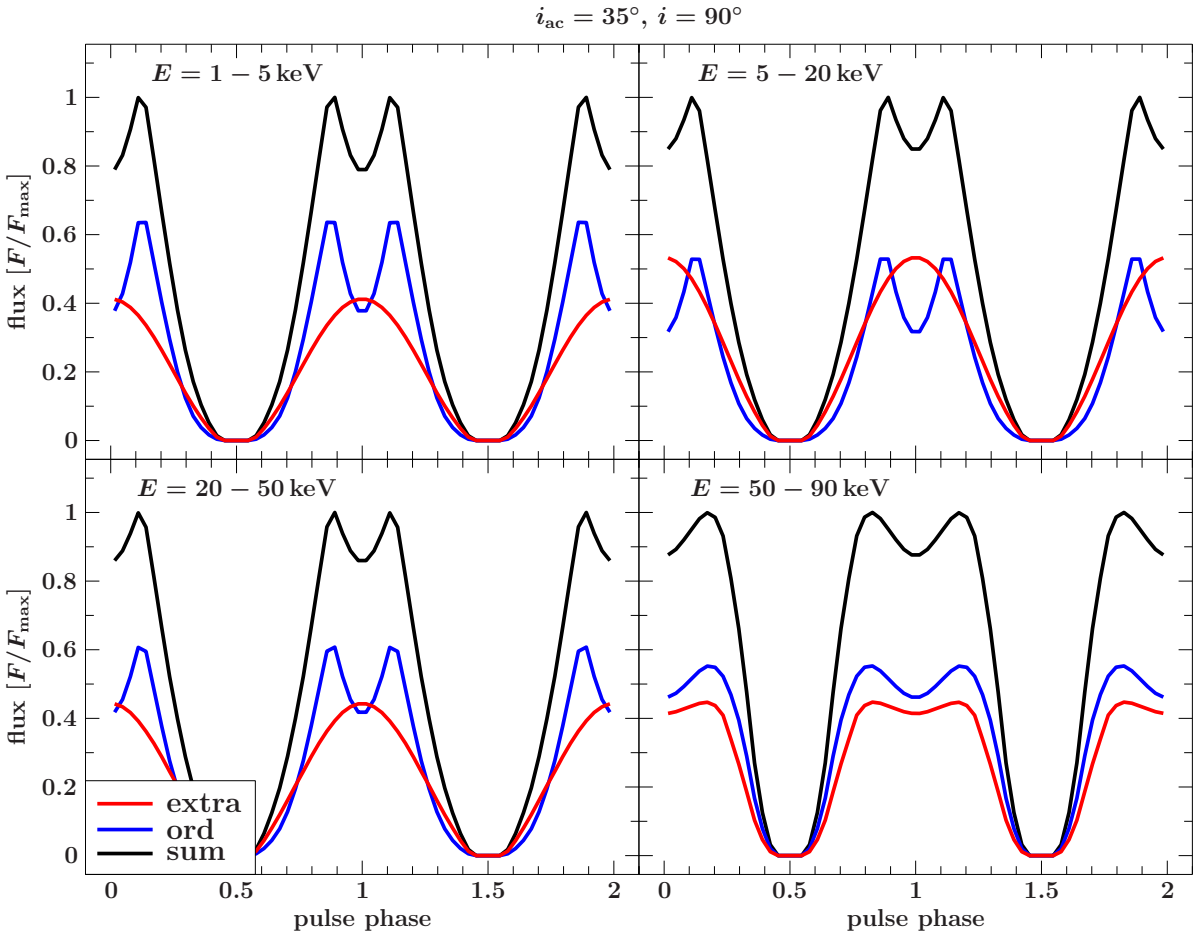

Figure 4.8: Pulse profile in 4 energy bands, with $i_{ac} = 35°$, $i = 90°$. The extraordinary, ordinary and the sum of both modes are indicated in red, blue, and black respectively. The physical parameters are as described in the beginning of this chapter.

is largely isotropic. This change causes the differences in the pulse profiles discussed above, e.g., the existence of two maxima in the 50–90 keV band of the extraordinary mode. Differences between the pulse profiles of the lower energy bands arise as a result of a relative change in the intensity of the modes and a slight variability in their emission profiles, as seen in Fig. 3.3 in chapter 3.

In conclusion, the energy dependence of the pulse profiles is crucial and therefore has to be taken into account when comparing the model to observations. This is especially important around the cyclotron line energy, where pulse profiles can differ greatly from what is seen in lower energy bands or the broad energy band.

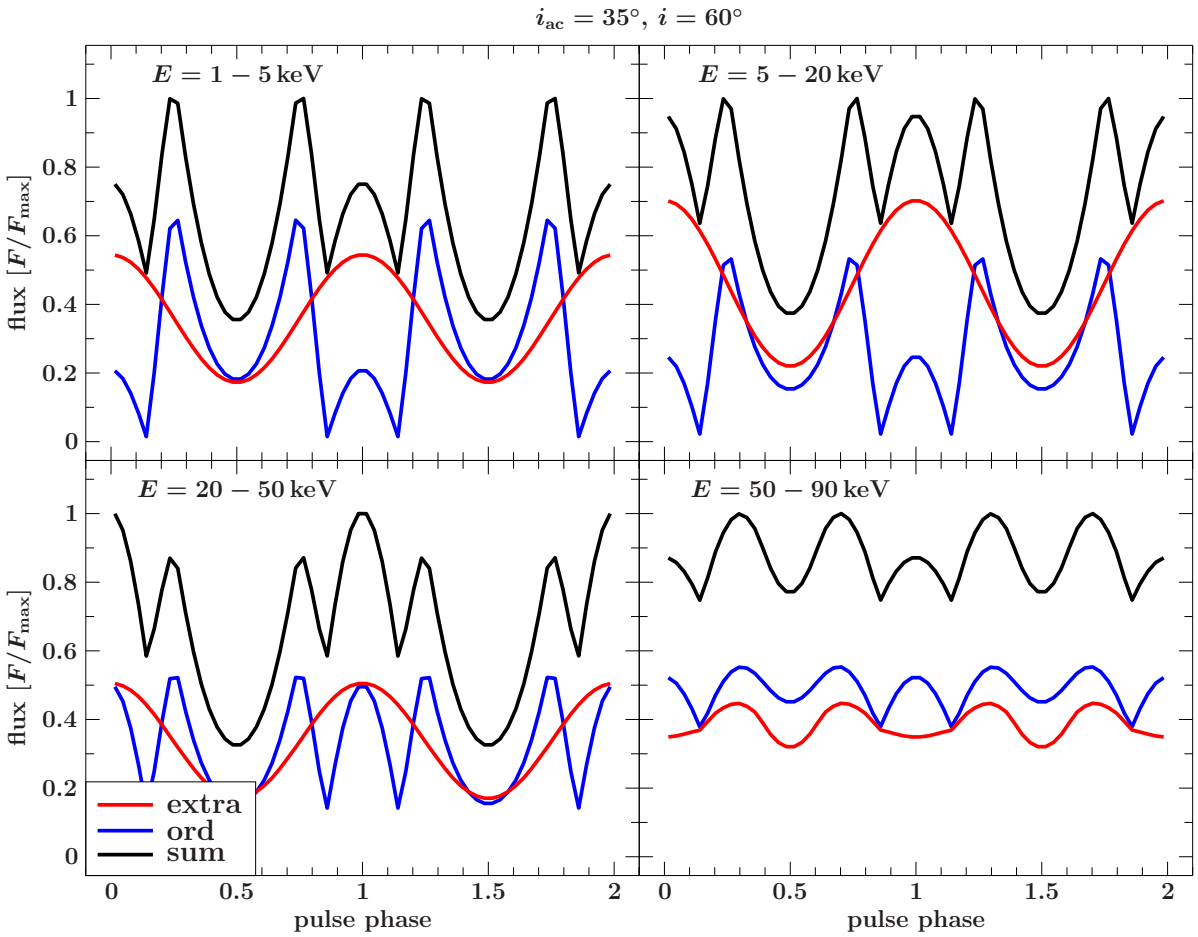

Figure 4.9: Pulse profile in 4 energy bands, with $i_{ac} = 35°$, $i = 60°$. The extraordinary, ordinary, and the sum of both modes are indicated in red, blue, and black respectively. The physical parameters are as described in the beginning of this chapter.

5 Summary and Conclusion

In this thesis, pulse profiles of X-ray pulsars with low accretion rates ($\dot{M} \lesssim 10^{15}\,\mathrm{g\,s^{-1}}$) have been modeled. The dependence of the pulse profiles on the observer inclination, i, the inclination of the hot spot, i_{ac}, and the polarization mode was investigated in four energy bands, ranging from 1–90 keV. The analysis is based on the `polcap` model (Sokolova-Lapa et al. 2019, in prep.), which describes polarized radiative transfer of thermal X-ray emission through a neutron star atmosphere, which is subject to heating and cooling due to interactions with the accreting matter. To account for relativistic light bending, the `LIBANS` code was used (Falkner 2012, 2018).

Pulse profiles show a complex behavior. Simple configurations, lsuch as a single hot spot seen from $i = 90°$, can lead to pulse profiles with multiple minima and maxima. This complexity is a consequence of the `polcap` emission profile, which peaks when seen directly from the top (central lobe), i.e., at a viewing angle of 0°, and at around ±50° (wings). This shape is a result of the directional dependence of the scattering and absorption cross sections, which arises due to Landau quantization in high magnetic fields.

Changes in i and i_{ac} result in a large variety of pulse profiles. The number of minima and maxima in the pulse profile depends on the emission profile and the observer's viewing angles on the hot spot, which are fixed by the choice of i and i_{ac}. Up to three maxima and minima arise during one rotation of the neutron star.

The emission profile is shaped by photons in the ordinary polarization mode, while the contribution from extraordinary photons is largely isotropic. This difference impacts the pulse profiles of these modes. It is therefore crucial to understand how each mode contributes to an observed pulse profile.

Electrons in the neutron star's atmosphere can scatter resonantly on Landau levels, which results in CRSFs in the spectra of X-ray pulsars and in a change of the `polcap` emission profile around the cyclotron energy, E_{cyc}. The pulse profile therefore depends on energy close to E_{cyc}. In addition, all other energy bands exhibit slightly varying pulse profiles.

The following paragraphs discuss the observational context of these results and highlight possibilities for future work.

Observations of X-ray pulsars at low accretion rates ($\dot{M} \lesssim 10^{15}\,\mathrm{g\,s^{-1}}$) are difficult, because they have low luminosities. Recently, Tsygankov et al. (2019a,b) observed the X-ray pulsars A 0535+262 and GX 341−1 at low accretion rates with the X-ray space telescope *NuSTAR*. Their analysis revealed a spectral shape with two humps, as predicted by

the `polcap` model. In the case of A 0535+262, Tsygankov et al. (2019a) investigated the pulse profile and found it to be similar to pulse profiles obtained at slightly higher luminosities. This result hints at a largely unchanged emission geometry in the range of observed luminosities ($7 \cdot 10^{34}$–$2 \cdot 10^{36}\,\mathrm{erg\,s^{-1}}$). Therefore, the `polcap` model might be valid up to slightly higher accretion rates than assumed here. However, a detailed pulse profile analysis has to be performed to falsify the results of this thesis. An important first step toward this goal would be the investigation of pulse profiles of GX 341–1 and A 0535+262, which can be obtained from the available *NuSTAR* data. A promising ansatz for further analysis is phase resolved spectroscopy, where the dependence of the spectrum on the pulse phase is studied.

On the theoretical side, an investigation of further parameters could prove promising, as well as a refinement of the `polcap` model (for details see Sokolova-Lapa et al. (2019, in prep.)). To date, the physical parameters of the `polcap` model can be varied in a narrow range. If this range is expanded, the influence of, e.g., the column depth, y_0, and the cyclotron energy, E_{cyc}, on the pulse profile can be investigated, which helps to pinpoint physical parameters in observations. In this thesis, pulse profiles originating from a single hot spot were modeled. From this simple setup, complex pulse profiles arise, which raises the question how more realistic field configurations affect the pulse profiles. In addition to the pulse profile, the spectrum and its dependence on the `polcap` parameters and the pulse phase can be investigated.

As shown in this thesis, the study of pulse profiles and spectra of accreting neutron stars provides a unique insight in their extreme environment, allowing us to study highly magnetized plasma and general relativity.

Acknowledgments

Ekaterina Sokolova-Lapa for her patience in explaining the physics behind this project and answering all my confused questions, especially during the proof reading.

Sebastian Falkner for his support with ISIS and Xfig. He always managed to rescue me out of the programming pitfalls I had maneuvered myself into.

Jörn Wilms for the opportunity to work on this project and to become a part of the Dr. Karl Remeis Observatory in Bamberg. His tips on writing style and LaTeX have been of great help.

Stefan Richter for his loving support and encouragement during the last weeks.

Bibliography

Becker, P. A., Klochkov, D., Schönherr, G., et al. 2012, Astronomy and Astrophysics, 544, A123

Becker, P. A. & Wolff, M. T. 2007, The Astrophysical Journal, 654, 435

Beloborodov, A. M. 2002, The Astrophysical Journal, 566, L85

Bhattacharya, D. & van den Heuvel, E. P. J. 1991, Physics Reports, 203, 1

Bissinger, M. 2016, PhD thesis, Dr. Karl Remeis-Sternwarte, Bamberg

Caballero, I. & Wilms, J. 2012, Memorie della Societa Astronomica Italiana, 83, 230

Falkner, S. 2012, Master's thesis, Dr. Karl Remeis-Sternwarte, Bamberg

Falkner, S. 2018, PhD thesis, Dr. Karl Remeis-Sternwarte, Bamberg

Ferrigno, C., Becker, P. A., Segreto, A., Mineo, T., & Santangelo, A. 2009, Astronomy & Astrophysics, 498, 825

Giacconi, R., Gursky, H., Kellogg, E., Schreier, E., & Tananbaum, H. 1971, The Astrophysical Journal, 167, L67

Giacconi, R., Gursky, H., Paolini, F. R., & Rossi, B. B. 1962, Physical Review Letters, 9, 439

Lai, D. 2001, Reviews of Modern Physics, 73, 629

Lamb, F. K., Pethick, C. J., & Pines, D. 1973, The Astrophysical Journal, 184, 271

Langer, S. H. & Rappaport, S. 1982, The Astrophysical Journal, 257, 733

Lattimer, J. M. 2012, Annual Review of Nuclear and Particle Science, 62, 485

Mihalas, D. 1978, Stellar atmospheres (Chicago, USA: The University of Chicago Press)

Mészáros, P. & Ventura, J. 1978, Physical Review Letters, 41, 1544

Pavlov, G. G., Shibanov, I. A., & Iakovlev, D. G. 1980, Astrophysics and Space Science, 73, 33

Pétri, J. 2019, Monthly Notices of the Royal Astronomical Society, 485, 4573

Schwarm, F.-W., Ballhausen, R., Falkner, S., et al. 2017a, Astronomy and Astrophysics, 601, A99

Schwarm, F.-W., Schönherr, G., Falkner, S., et al. 2017b, Astronomy & Astrophysics, 597, A3

Sokolova-Lapa, E., Gornostaev, M., Wilms, J., et al. 2019, Astronomy & Astrophysics in prep.

Staubert, R., Trümper, J., Kendziorra, E., et al. 2019, Astronomy and Astrophysics, 622, A61

Tananbaum, H., Gursky, H., Kellogg, E. M., et al. 1972, The Astrophysical Journal, 174, L143

Truemper, J., Pietsch, W., Reppin, C., et al. 1978, The Astrophysical Journal, 219, L105

Tsygankov, S. S., Doroshenko, V., Mushtukov, A. A., et al. 2019a, Monthly Notices of the Royal Astronomical Society, 487, L30

Tsygankov, S. S., Rouco Escorial, A., Suleimanov, V. F., et al. 2019b, Monthly Notices of the Royal Astronomical Society, 483, L144

Wang, J. C. L., Wasserman, I. M., & Salpeter, E. E. 1988, The Astrophysical Journal Supplement Series, 68, 735

Zhang, C. M. & Kojima, Y. 2006, Monthly Notices of the Royal Astronomical Society, 366, 137

Eidesstattliche Erklärung

Ich versichere hiermit, die von mir vorgelegte Arbeit selbstständig verfasst zu haben. Alle Stellen, die dem Wortlaut oder dem Sinn nach aus veröffentlichten oder unveröffentlichten Werken anderer entnommen sind, wurden als solche gekennzeichnet. Sämtliche für die Anfertigung der Arbeit genutzten Quellen und Hilfsmittel sind angegeben. Diese Arbeit hat mit gleichem Inhalt bzw. in wesentlichen Teilen noch keiner anderen Prüfungsbehörde vorgelegen.

Bamberg, 17. September 2019

.....
(Lucia Härer)